Marine and Petroleum Geology 147 (2023) 105984

Contents lists available at ScienceDirect

Marine and Petroleum Geology

journal homepage: www.elsevier.com/locate/marpetgeo

Reservoir heterogeneity of an Eocene mixed siliciclastic-carbonate succession, northern Pannonian Basin

Sándor Körmös [a,b,*], Andrea Varga [a], Béla Raucsik [a], Georgina Lukoczki [c], Balázs Géza Radovics [b], Nikoletta Papp [a], István Futó [d], Félix Schubert [a]

[a] University of Szeged, Department of Mineralogy, Geochemistry and Petrology, Egyetem u. 2, H-6722, Szeged, Hungary
[b] MOL Plc, Október Huszonharmadika u. 18, H-1117, Budapest, Hungary
[c] University of Kentucky, Kentucky Geological Survey, 504 Rose Street, Lexington, KY, 40502, USA
[d] Institute for Nuclear Research, Isotope Climatology and Environmental Research Centre, Bem Tér 18/c, H-4026 Debrecen, Hungary

ARTICLE INFO

Keywords:
Reservoir heterogeneity
Mixed siliciclastic-carbonate succession
Diagenetic evolution
Multiphase hydrocarbon emplacement
Porosity enhancement and degradation
Hungarian Palaeogene Basin

ABSTRACT

The quality of any reservoir is strongly controlled by diagenetic processes, especially of those that are comprised of mixed siliciclastic-carbonate sequences. An Eocene mixed siliciclastic-carbonate sequence forms reservoirs with diverse reservoir quality in the Hungarian Palaeogene Basin, which is found within the Pannonian Basin. Late Eocene transgression established extensive shallow-marine depositional environments strongly controlling the early diagenetic processes. Drill cores and cuttings were selected from several boreholes, representing a wide range of lithofacies to reveal the cause for reservoir heterogeneity. Petrographic, stable isotope and fluid inclusion analyses were performed to identify the diagenetic processes that controlled the porosity evolution of the reservoir, The early diagenetic calcite neomorphism caused lateral homogeneity, whereas the early meteoric water incursion enhanced reservoir properties *via* the development of dissolution pores, which in turn resulted in vertical reservoir heterogeneity. The deterioration of porosity started in the eogenetic realm by kaolinite formation and continued during mesodiagenesis as burial calcite, quartz, dolomite and minor illite cement precipitated in remaining pore spaces. Petrographic evidence, such as kaolinite transformation into dickite and fluid inclusion homogenisation temperatures highlight the role of temperature increase with burial, the effect of changing fluid chemistry during the evolution of the basin is documented by the chemical zonation of dolomite, the variation in salinities of the fluids enclosed fluid inclusions, as well as recurrent and prolonged periods of cementation with calcite, quartz and dolomite. Mesogenetic processes were accompanied by hydrocarbon emplacement and the formation of late-stage pyrite. The propagation and cementation of faults first contributed to increase and later to reduce fluid flow, respectively. These steps collectively resulted in a heterogeneous reservoir, characteristic of the Eocene sequence in the Hungarian Palaeogene Basin.

1. Introduction

Clastic and carbonate reservoirs have been extensively investigated over the last century and the findings have been summarized in numerous special publications (e.g., Burley and Worden, 2003; Flügel, 2004; Lucia, 2007; Pettijohn et al., 1973; etc.). However, mixed siliciclastic-carbonate deposits earned less attention until recent years (e.g., Chiarella et al., 2017; Du et al., 2022; Feng et al., 2013; Mansurbeg et al., 2009; Palermo et al., 2008). In such deposits, carbonate and siliciclastic constituents act differently during diagenesis, which results in remarkable lateral and vertical reservoir heterogeneity. These mixed sediments may undergo a more extensive porosity loss compared to pure siliciclastic ones due to more pronounced compaction and cementation in the former (Mansurbeg et al., 2009). However, the dissolution of carbonate grains may enhance the reservoir capacity in a mixed siliciclastic-carbonate strata (Feng et al., 2013). This special type of sedimentary rock may host high-quality reservoirs, such as the Rogenstein Member of Lower Buntsandstein Formation in western Europe (Palermo et al., 2008) or the Shahejie Formation in the Bohai Bay Basin in China (Du et al., 2022).

In the Pannonian Basin, there are six known petroleum systems. The Palaeogene petroleum system of the Hungarian Palaeogene Basin,

* Corresponding author.University of Szeged, Department of Mineralogy, Geochemistry and Petrology, Egyetem u. 2, H-6722, Szeged, Hungary.
E-mail address: sandor.kormos@geo.u-szeged.hu (S. Körmös).

https://doi.org/10.1016/j.marpetgeo.2022.105984
Received 28 August 2022; Received in revised form 17 October 2022; Accepted 18 October 2022
Available online 22 October 2022

located in the north-central part of Hungary, is one of the most complex of these petroleum systems (Fig. 1a; Dolton, 2006). The studied area is in the south-central part of the Hungarian Palaeogene Basin where several exploration and development wells were drilled in recent years. The wells penetrated more than two thousand meters of Neogene and Palaeogene sediments to reach the Mesozoic basement. The selected wells, W–1, W–7, W–9, W–14 and W–15 (Fig. 1b), penetrated Eocene mixed siliciclastic-carbonate hydrocarbon reservoirs with variable reservoir quality. Available reports point out the difficulty of production from these reservoirs (Boncz, 2013; Radovics et al., 2017). Diagenetic processes fundamentally influence rock characteristics that in turn constrain the volume in place estimation or long-term production capability of the reservoir, among others. Diagenesis also controls reservoir heterogeneity, causing compartmentalisation or, in a worst case, shortens the duration of production. Therefore, it is crucial to understand the diagenetic history of a heterogeneous mixed siliciclastic-carbonate system to be able to predict the reservoir quality. To maintain favourable production capacity, a detailed investigation of diagenetic processes characterising the Eocene mixed siliciclastic-carbonate reservoir rocks and their surroundings is needed as prerequisite for appropriate reservoir description. Thus, the goal of this study is to enhance the understanding of the diagenetic processes that control the quality of the mixed siliciclastic-carbonate reservoirs in the Hungarian Palaeogene Basin. To achieve this goal, optical petrography, qualitative and semi-quantitative analysis of the mineral phases, stable isotope and fluid inclusion analyses were performed, which revealed how the depositional environment controlled early diagenetic processes, and how the thermal history of the basin, together with the chemical evolution of fluids that migrated in the basin during mesogenesis, resulted in the complex reservoir characteristics encountered today.

2. Geological setting

The study area is located in the south-central part of the Hungarian Palaeogene Basin (Fig. 1). The rocks of this basin overlie the pre-Cenozoic basement rocks that comprise the Mid-Hungarian Zone (Kovács and Haas, 2010). The Hungarian Palaeogene Basin was formed in a retro-arc flexural foreland basin, where the paleo-depositional facies were reconstructed to have migrated ENE-ward during the Cenozoic (Tari et al., 1993; Kováč et al., 2016). The tectonic evolution of the Hungarian Palaeogene Basin was controlled by normal faulting and strike-slip movements (Palotai, 2013 and references therein). The Palaeogene Basin as a term includes all sedimentary sequences related to the depositional cycle from the Eocene to the Early Ottnangian (Sztanó and Tari, 1993).

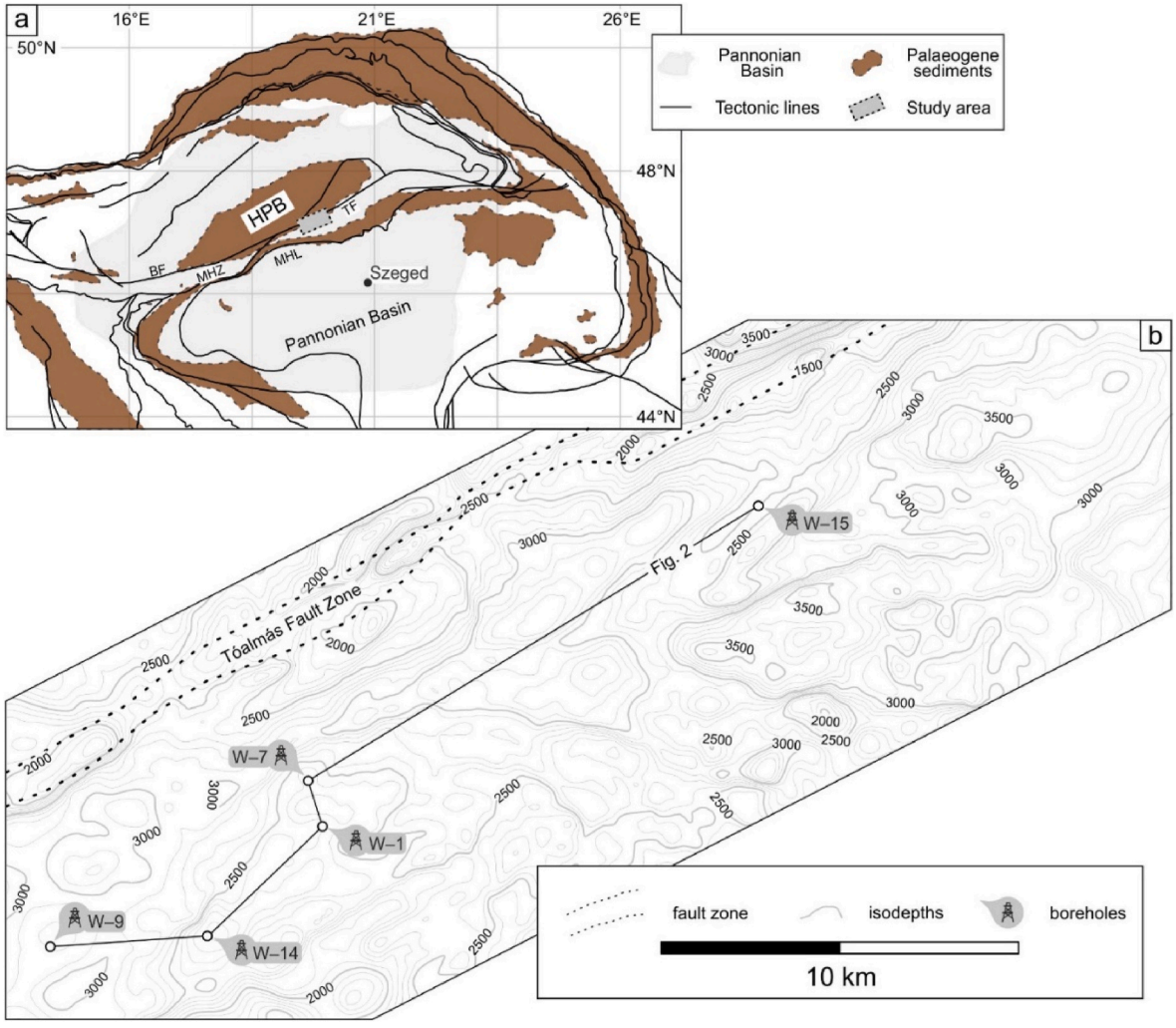

Fig. 1. Map of the study area. a) Regional setting of the Hungarian Palaeogene Basin (modified after Kováč et al., 2016; Ozsvárt et al., 2016; Palotai, 2013; Schmid et al., 2008). b) Map showing the top of the pre-Cenozoic basement in the study area (modified after Boncz, 2013). Values, printed on isodepths, represent depths in metre below sea level. HPB – Hungarian Palaeogene Basin, BF – Balaton Fault, MHZ – Mid-Hungarian Zone, MHL – Mid-Hungarian Line, TF – Tóalmás Fault, W–1 to W–15 are the studied boreholes.

The pre-Cenozoic basement of the research area is composed of Mesozoic rocks from different structural mega-units. The western part of the basement is comprised of Ladinian to Norian platform carbonates (Haas and Kovács, 2012) very similar to those of the Buda Hills (Transdanubian Range Unit). In the east, besides the Ladinian to Norian platform carbonates, a deep marine Middle to Upper Jurassic sedimentary succession and magmatites (Pelikán, 2005) are also reported showing pronounced affinity to the sequence of the Bükk Mountains (Bükk Unit).

In this area, the Alpine orogeny culminated in the exhumation of the Mesozoic strata during the Late Cretaceous and led to continental denudation that lasted until the Late Eocene (Haas and Kovács, 2012). Thus, the Palaeogene sediments overlie the Mesozoic basement on top of a regional unconformity (Fig. 2). The sedimentary succession starts with terrigenous conglomerate, breccia and variegated claystone (Bauer et al., 2016). The Kosd Formation reflects the development of a lagoonal environment (Gidai, 1978; Less, 2005), preserving the sign of the Priabonian transgression (Fig. 2b and c; Báldi and Báldi-Beke, 1985). The coal-bearing upper part of the Kosd Formation includes pelitic sediments with variable carbonate content (Gidai, 1978; Less, 2005; Körmös et al., 2020). The shelf deposits of the Szépvölgy Limestone Formation overlie the Kosd Formation (Fig. 2a; Kázmér, 1985). Extended periods of subsidence resulted in the deposition of the Buda Marl Formation (Fig. 2a), containing marl and calcareous marl, allodapic limestones and calcareous turbidites deposited during the Eocene–Oligocene transition under oxygen-depleted conditions (Less, 2005; Nagymarosy and Báldi-Beke, 1988; Ozsvárt et al., 2016).

The Buda Marl Formation is covered by the Tard Clay Formation (Fig. 2a), which accumulated in a euxinic basin, and was later filled up from the west (according to the present position; Fodor et al., 1994) by prograding siliciclastic deltas. The Tard Clay Formation contains laminated and massive shale and sandstone (Brukner-Wein et al., 1990). The overlying sediments accumulated in a deep bathyal, well-oxygenated depositional environment (Báldi and Báldi-Beke, 1985), comprising the Kiscell Clay Formation (Fig. 2a), which is characterised by intercalations of siltstones and turbiditic sandstone bodies (Less, 2005; Milota et al., 1995).

The Palaeogene succession ends by interfingering heteropic sediments, including the shallow sublittoral Törökbálint Sandstone Formation, the deep sublittoral–shallow bathyal Szécsény Schlier Formation and the deep sublittoral Eger Formation (Fig. 2a; Kercsmár et al., 2015). The littoral–sublittoral Budafok Formation covers the Törökbálint Sandstone, which is laterally intercalated with the upper part of the Szécsény Schlier Formation (Fig. 2a; Sztanó and Tari, 1993). The latter grades eastwards into the shallow marine Pétervására Sandstone Formation, composed of several coast-parallel facies units (Fig. 2a; Sztanó and Tari, 1993). Gradual uplift in late Eggenburgian time resulted in subaerial exposure and the deposition of the Zagyvapálfalva Formation (Fig. 2a) in a coastal plain setting. The Gyulakeszi Rhyolite Tuff covers the eroded surface of the Palaeogene to Eggenburgian formations

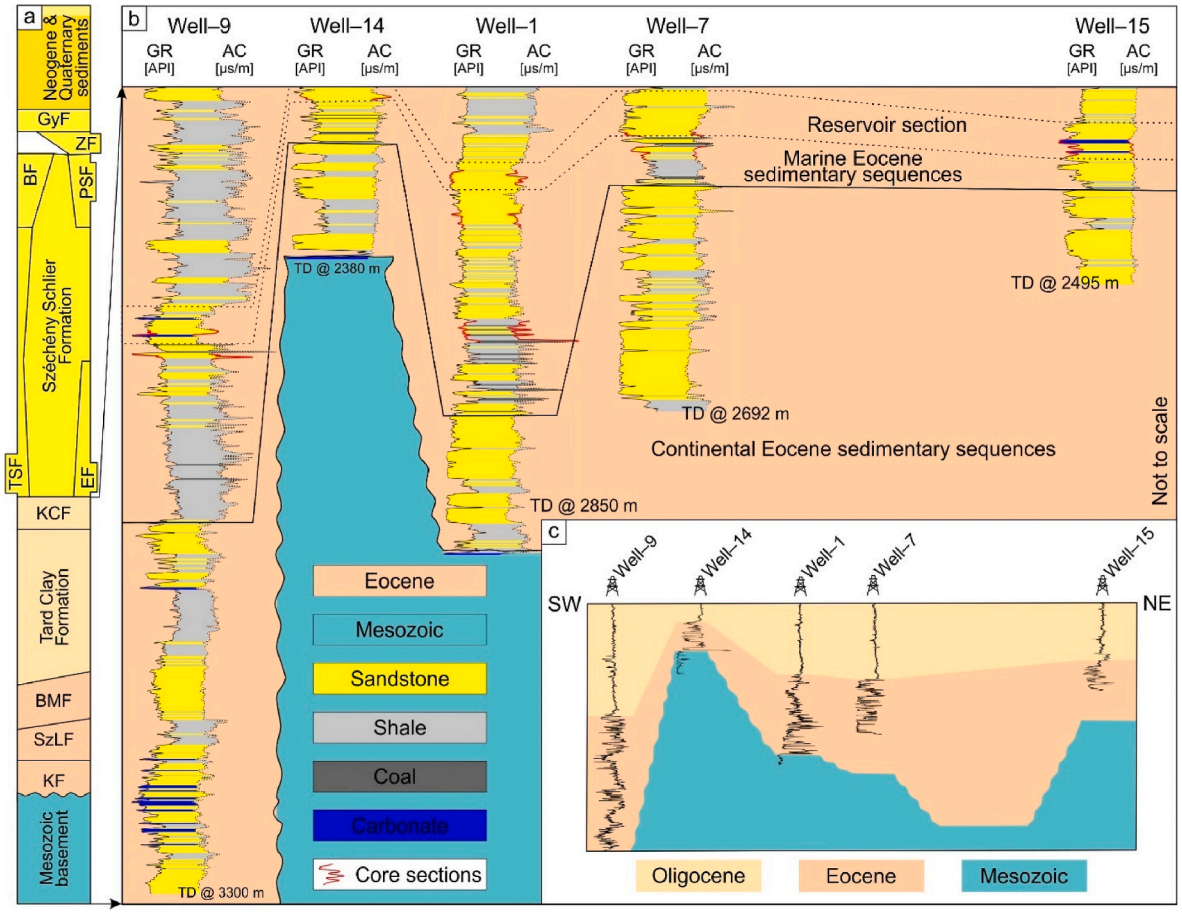

Fig. 2. Schematic stratigraphic diagrams of the study area. a) Interpreted lithostratigraphic chart of the Hungarian Palaeogene Basin and stratigraphic section along the investigated boreholes (for locations see Fig. 1) based on well logs b) gamma ray and acoustic, the top level of the section flattened along the top of the Eocene, and c) gamma ray log, levelled out along the top of the Oligocene. Red curves indicate cored intervals studied. KF – Kosd Formation, SzLF – Szépvölgy Limestone Formation, BMF – Buda Marl Formation, KCF – Kiscell Clay Formation, TSF – Törökbálint Sandstone Formation, EF – Eger Formation, BF – Budafok Formation, PSF – Pétervására Sandstone Formation, ZF – Zagyvapálfalva Formation, GyF – Gyulakeszi Formation, GR – gamma ray log, AC – acoustic log, TD – total depth. (For interpretation of the references to colour in this figure legend, the reader is referred to the Web version of this article.)

(Fig. 2a; Nagymarosy, 2012). The sedimentary sequence of the Hungarian Palaeogene Basin is covered by thick Neogene sediments (Fig. 2a).

3. Samples and analytical methods

3.1. Samples

Boreholes, including W–1, W–7, W–9, W–14 and W–15, were drilled by MOL Plc. during the last decades (for locations see Fig. 1). In total, 200 m of drill core and 2200 m of drill cuttings were collected to characterise the diagenetic evolution of the Eocene mixed siliciclastic-carbonate sequence. The selected drill cores and drill cuttings represent a wide range of lithofacies (Fig. 2b and c).

3.2. Analytical methods

A total of 50 representative drill core samples were impregnated with blue epoxy prior to thin section preparation. Thin sections made of these samples and an additional 24 covered archive thin sections were studied using an Olympus BX41 and a Brunel SP300P polarisation microscope for petrographic and modal analyses. The Gazzi-Dickinson point-counting method (Ingersoll et al., 1984) was used for modal analysis of sandstones considering at least 400 points. Dott (1964) and Mount (1985) classifications were followed for the discrimination of sandstones. Petrographic descriptions of grain and matrix content were performed by visual comparison of percentage (Folk, 1951), roundness (Powers, 1953) and sorting charts (Harrel, 1984; Jerram, 2001). Representative samples were selected and stained with a solution of alizarin red-S and potassium ferricyanide to distinguish non-ferroan and ferroan calcite and dolomite (Dickson, 1965).

A Reliotron VII cold-cathode cathodoluminescence (CL) device assembled on an Olympus BX43 polarizing microscope equipped with an Olympus DP73 digital camera was used for CL microscopy of thin sections to further characterise the authigenic minerals. The operating settings were 7 kV accelerating voltage and 670 μA beam current.

X-ray powder diffraction measurements were performed for qualitative and semi-quantitative analysis of the mineral phases in sandstone and siltstone samples. A total of 10 representative bulk samples were taken and ground in an agate mortar to about 10 μm grain size. Before separation of the clay (grain size of <2 μm) fraction, calcium-carbonate content of the samples was digested by 10 vol% acetic acid solution at room temperature and decanted repeatedly until pH 6 was reached. Subsequently, the clay fraction was separated by repeated ultrasonic deflocculation and gravitational settling. Oriented clay specimens were made by pipetting on glass slides and drying at 50 °C. Both the homogenised bulk samples and air-dried clay specimens were measured on standard sample holders using a Rigaku Ultima IV X-ray diffractometer (CuKα radiation, Bragg-Brentano geometry, secondary graphite monochromator, proportional counter, divergence and detector slits of 2/3°). Thereafter, in order to detect swelling phases, the clay specimens were solvated by ethylene-glycol at 60 °C for 16 hrs and measured. As next steps, the specimens were heat-treated (at 350 °C and 550 °C) and measured. The random bulk samples were scanned at 50 kV/40 mA with 3–70° 2Θ diffraction angle range, step-scan 0.05° 2Θ and 1°/min scan speed. The oriented clay specimens (air-dried, ethylene-glycolated and heat-treated) were measured at 45 kV/35 mA, from 3° to 50° 2Θ with a goniometer step-width of 0.1° 2Θ and 1°/min step rate. Polytypism of the clay minerals were established using random clay specimens on 'zero background' Si sample holder with 15–60° 2Θ scan range, 0.02° 2Θ step size and 0.5°/min scan speed. Qualitative interpretation of the samples was done using the International Centre for Diffraction Data database of Rigaku PDXL 1.8 software. Semi-quantitative compositions of the bulk samples were determined by the reference intensity ratio method. The semi-quantitative composition of the clay fraction was estimated by the integrated area of the conventionally used basal reflections and correction factors of Poppe et al. (2001).

Scanning electron microscopy was applied for the characterisation of pore-filling minerals. Fifteen freshly broken, approximately 1 cm^3 rock fragments and thin sections were gold coated and analysed by a Hitachi S-4700 field emission scanning electron microscope combined with a Bruker (former Röntec) QX2 energy dispersive X-ray fluorescence spectrometer. The analysis was carried out at 20 kV acceleration voltage and 9 μA beam current.

Stable carbon and oxygen isotope measurements of 25 representative samples of mold-filling and vein-forming calcite and bulk rocks were performed on hand-drilled powders. The pulverized samples were solvent extracted, using 20 ml chloroform, acetone then ethanol in two runs, to avoid contamination caused by solid bitumen and oil stain. Milli-Q water was used to flush the calcite and rock powders, and those were dried in an oven at 60 °C. The samples were analysed using a continuous flow technique with the H_3PO_4 digestion method (Spötl and Vennemann, 2003). The isotope ratios of CO_2, generated by acid reaction, were measured using a Thermo Finnigan DELTA plus XP IR mass spectrometer through a GasBench interface. Stable isotope ratios are expressed relative to the Vienna Pee Dee Belemnite standard (V-PDB) in delta notation ($\delta = [R_{sample}/R_{standard} - 1) \times 1000$; Coplen (2011), where R is ($^{13}C/^{12}C$) or ($^{18}O/^{16}O$). The delta notation is reported in per mil (‰). The analytical error during the measurements was better than 0.1‰.

For the fluid inclusion (FI) study, representative samples containing authigenic minerals (calcite, dolomite and quartz) were chosen, including one cm-sized pore-filling and one fracture-filling calcite sample, three sandstone samples (two arenites and one wacke), one siltstone drill core sample, and one sample made from drill cuttings. A total of seven double-polished 50–80 μm thick sections were prepared according to Shepherd et al. (1985). For cutting the samples a low-speed saw was used to avoid thermal or mechanical damage of FIs. Fluid inclusion petrography, microthermometry, UV-fluorescence and Raman microspectroscopy were performed on these thick sections.

Fluid inclusion assemblages (FIAs) were characterised following the instructions of Goldstein and Reynolds (1994). Linkam MDSG-600 and THMSG-600 heating-freezing stages mounted on an Olympus BX41 polarizing microscope were used for microthermometry. Synthetic FIs were measured for calibration purposes at −56.6 °C, 0.0 °C and 374.0 °C. The accuracy of the measurements was ±0.2 °C below 100 °C and ±1.0 °C above 100 °C. Fluid inclusions that show petrographic evidence of necking down were left out of measurements. To avoid stretching of aqueous FIs caused by freezing of the liquid phase, heating analyses were performed before freezing. A stepwise 1 °C heating rate was applied for accurate observation of phase changes while cross-checking the FIs. Terms and symbols suggested by Diamond (2003) were used during the study. The temperatures of homogenisation (T_h) and final ice melting (T_m(Ice)) were determined by the cycling method (Goldstein and Reynolds, 1994). Volume fractions of the vapour and liquid phases (φ_V) were estimated at room temperature. Salinity values of aqueous inclusions (AI) were calculated by final ice-melting temperatures and reported in mass percent (mass%) of NaCl equivalent (Bodnar, 1993; Bakker, 2003). In the present study, methane was detected in the vapour phase of some fluid inclusions, but methane hydrate was not observed upon cooling to −160 °C. Therefore, the reported salinities are assumed as maximum salinity values (e.g., Fall et al., 2011; Ou et al., 2015) because the concentration of the gaseous hydrocarbons in the AI could not be determined.

UV-fluorescence micro-spectroscopy was utilized to characterise the hydrocarbon-bearing FIs (HCFI). An Olympus BX41 polarizing microscope equipped with a 100 W high-pressure Hg lamp and an Olympus U-MNU-2 filter set for ultraviolet (360–370 nm) and Olympus U-MWBV2 filter set for blue-violet (400–440 nm) excitation was used for analysis. The spectra were recorded by an Ocean Optics QE PRO spectrometer connected through a QP115-025-XSR optical fibre to the microscope. For optimization of signal to noise ratio, the spectra were recorded

during 1500 msec, using three times spectrum averaging and two times boxcar width on a spot of 2 μm diameter. Dark and white backgrounds were acquired at every crystal hosting HCFI to avoid colour-shifting caused by the refraction of the host mineral. The comparison between different petroleum types was done by the transformation of each spectrum to XYZ chromaticity coordinates and was plotted on CIE-1931 (Commission Internationale d'Eclairage) chromaticity chart (Smith and Guild, 1931).

Raman spectroscopy was applied to identify the volatile phases of the FIs. The measurements were carried out on a Thermo Scientific DXR confocal Raman microscope. A frequency-doubled diode-pumped solid-state Nd-YAG 532 nm wavelength laser with a 100× objective lens at 5 mW laser power was used. The spectral resolution of the instrument was 2 cm^{-1}, while the spatial resolution was 3–4 μm^3. Acquisition time was set to 1500 msec for obtaining the best signal to noise ratio. The Raman shifts were compared to the results of Frezzotti et al. (2012) for qualitative results.

4. Results

4.1. Mineralogy of the eocene sediments

The mineralogical composition of the bulk rock samples is characterised by variable amounts of quartz, 10Å phases (illite ± mica), calcite, and 7Å phase (kaolin-group minerals) as major components (Table 1). In some samples, the calcite and the 7Å phase can be detected only in trace amounts. Besides these, potassium feldspar, plagioclase, dolomite and pyrite also occur in trace amounts. In a few samples, dolomite and pyrite were each measured to comprise up to 5–10% of the sample.

Sst – sandstone, Sltst – siltstone, qtz – quartz, pl – plagioclase feldspar, kfp – K-feldspar, cal – calcite, dol – dolomite, 10Å – 10 Ångström phase (illite ± mica), 7Å – 7 Ångström phase (kaolin-group minerals), ill/sm – highly swelling mixed-layer illite/smectite, pyr – pyrite, $PT_{10Å}$ – polytypes of the 10 Ångström phase, $PT_{7Å}$ – polytypes of the 7 Ångström phase, kln > dck – kaolinite is more abundant than dickite, dck > kln – dickite is more abundant than kaolinite, dck ≈ kln – not possible to distinguish which polytype is more abundant, tr – trace amount. Percentage values for the 10Å and 7Å phases in the clay fraction express possible maximum amounts.

The clay (<2 μm-sized) fractions of siltstone and sandstone samples are generally predominated by 10Å phases (illite ± mica). Nevertheless, the 7Å phase is also an important component and it is the major clay mineral in one studied sample. The illite ± mica is represented by the $2M_1$ polytype. As for the kaolin polytypes, in some samples, kaolinite prevails over dickite but mostly dickite predominates over kaolinite. Besides these, minor mixed-layer illite/smectite is also present in most samples and, due to its very limited abundance, it cannot be quantified in a satisfactory manner. Trace amounts of quartz and pyrite are also identified in all analysed samples (Table 1).

4.2. Petrography of the eocene sedimentary rocks

The investigated core samples contain consolidated siltstones, sandstones and conglomerates (Appendix A). Siltstones are generally medium grey, interbedded with light grey sandstones, showing flaser-to-wavy-beddings, which are often destroyed by bioturbation. Besides the wavy-bedding, slumps also occur. The flaser-to-wavy-bedded siltstones are interrupted by erosional scour surfaces. Sandstones are fine-to-medium-grained, thin-to-thick-bedded, structureless and dominated by the alternation of light grey, calcareous and brownish grey, crude oil-impregnated lithotypes. Conglomerates are grain-supported and oligomictic, containing metamorphic and carbonate granules and pebbles.

4.2.1. Framework grains of the sandstones

The framework of the samples is built up of quartz (51–99%), feldspar (0–5%) and lithic fragments (1–49%; Fig. 3). The results of point counting are presented in Appendix B. The grains are angular to subrounded and show low to medium sphericity. The range of the grain size is typically between the coarse silt and medium sand and it is locally coarse-grained. The samples are poorly to moderately sorted and contain up to 30% of the argillaceous and calcareous matrix. The representative textures are presented in Fig. 4. The sandstones are classified as quartz and lithic arenites and wackes (Fig. 3a; Dott; 1964). Based on the high proportion of calcareous matrix, the wackes are further categorised as sandy micrite and micritic sandstone (Fig. 3b; Mount; 1985).

Detrital quartz grains dominantly are monocrystalline, and rarely show undulose extinction (>5°). Polycrystalline quartz grains are present in lower quantities and the boundary between the crystals within the grains is straight or sutured. As the grain size decreases the proportion of monocrystalline quartz grains increases in the samples. Feldspars are not common but potassium feldspar and plagioclase locally occur. In most cases, feldspars are replaced by calcite and clay minerals. Lithic grains are also important constituents and are dominated by metamorphic grains. Besides these, minor amounts of carbonate, chert, mudstone/shale, sandstone and volcanic (cf. Ingersoll et al., 1984) rock fragments are also present in the samples.

Besides the detrital framework grains, up to mm-sized detrital muscovite and locally, up to 3-mm-long elongated metamorphic granules are present in the samples. Mica flakes are common in the very fine-to-fine-grained sandstones and form a major component of those samples. The sandstones are rich in fossils preserved in varying degrees, including nummulites, miliolid foraminifers, molluscs, brachiopods, echinoids, red algae and bryozoans (Figs. 4–6; Appendices A and C). In some cases, the skeletal grains are identified based on their micritic envelopes and are replaced by pyrite, kaolinite and ferroan calcite. Accessories, such as heavy minerals, including rutile and tourmaline, occur in the sandstones and siltstones.

The framework grains in the wackes float in the calcareous matrix (microspar), or are in tangential contact, whereas, in the arenites

Table 1
Semi-quantitative mineralogical composition of selected samples from W–1 well.

	Bulk rock								Clay (<2 μm-sized) fraction						
	qtz	pl	kfp	cal	dol	10Å	7Å	pyr	ill/sm	10Å	$PT_{10Å}$	7Å	$PT_{7Å}$	qtz	pyr
	[%]								[%]			[%]		[%]	
Sst	40–50	–	–	30–40	–	10–20	5–10	tr	–	65	$2M_1$	35	dck > kln	tr	tr
	50–60	–	–	10–20	tr	10–20	tr	tr	–	73	$2M_1$	27	kln > dck	tr	tr
Sltst	20–30	–	–	5–10	tr	50–60	5–10	tr	tr	72	$2M_1$	28	dck > kln	tr	tr
	40–50	–	tr	tr	tr	40–50	tr	tr	–	88	$2M_1$	12	dck > kln	tr	tr
	40–50	tr	–	tr	tr	40–50	tr	tr	tr	74	$2M_1$	26	dck > kln	tr	tr
	60–70	tr	–	5–10	tr	10–20	tr	tr	tr	79	$2M_1$	21	dck ≈ kln	tr	tr
	60–70	tr	–	–	–	10–20	5–10	tr	tr	29	$2M_1$	71	dck ≈ kln	tr	tr
	30–40	tr	–	–	–	40–50	5–10	5–10	tr	70	$2M_1$	30	dck > kln	tr	tr
	40–50	tr	–	5–10	5–10	20–30	tr	tr	tr	82	$2M_1$	18	dck ≈ kln	tr	tr
	20–30	tr	–	tr	tr	50–60	5–10	tr	tr	80	$2M_1$	20	kln > dck	tr	tr

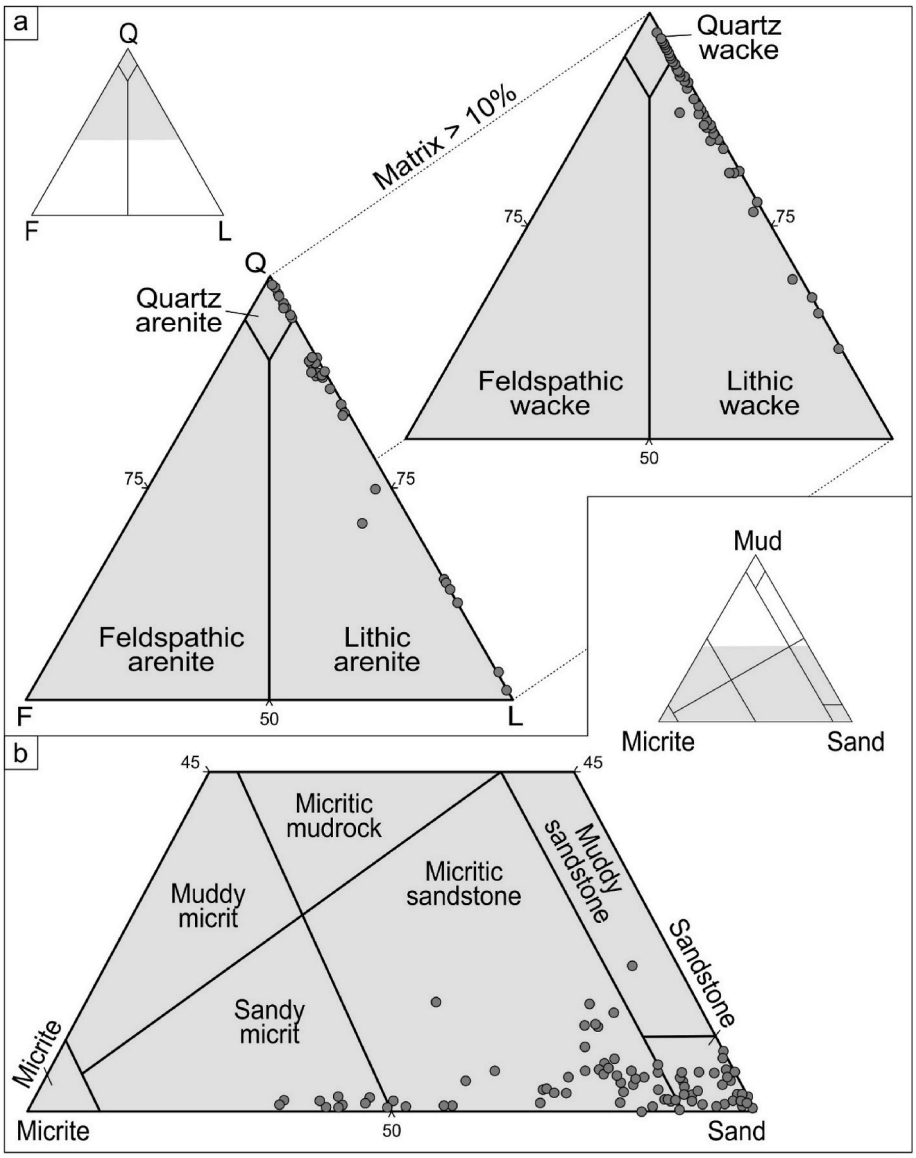

Fig. 3. Modal composition and classification of the sandstones. a) Framework grain composition (modified after Dott, 1964). b) Normalised composition of the mud, micrite and sand fraction (modified after Mount, 1985). Q – quartz grains, F – feldspar grains, L – lithic fragments.

tangential to long and concavo-convex contacts also occur (Fig. 4). Micas are commonly bent and the flakes are split apart (Appendix Ce). The rigid quartz grains squeeze and break bioclasts (Fig. 4a). Microstylolites, when present, either cross-cut the samples over several centimetres or cease within a few millimetres (Appendix Ca and b). Besides these, further evidence of pressure solution, such as dissolution pits, are also documented in detrital quartz grains (Fig. 7). In some samples, mica flakes, elongated pebbles and fossil fragments are oriented parallel along their long axis.

4.2.2. Diagenetic minerals

Authigenic minerals occur as grain coatings, replacement and pore-filling phases, including illite/smectite, pyrite, calcite, dolomite, quartz and kaolin minerals. Table 2 summarizes the occurrence of diagenetic minerals in the different lithotypes.

4.2.2.1. Calcite. Calcite occurs either as a pervasive ferroan microspar (Fig. 4c), showing dull orange CL in the wackes, embaying the framework grains, or it forms up to medium-and-coarse-crystalline elongated, drusy, equant and blocky ferroan calcite spar in the sandstones. The coarse spar locally embays multiple grains, forming a poikilotopic fabric (Fig. 5a and b) or heals cm-wide fractures (labelled later as Cal_{FF}, see section 4.3.1.; Appendix Cd). Drusy mosaics or locally single euhedral crystals of calcite occlude the chambers of well-preserved bioclasts and oversized pores (labelled later as Cal_{EU}, see section 4.3.1.; Fig. 5c). Equant spar seals partially the intergranular pores, molds and locally develop in equidistance in the molds of fossil fragments (labelled later as Cal_{EQ}, see section 4.3.1.; Fig. 5c). The calcite spars are characterised by distinct CL features and show bright and dull orange luminescence with locally developed zoning, but non-luminescent sparry calcite also exists (Fig. 5a and b). Locally, the CL-zoned calcite also shows zoning under UV and blue-light irradiation (Fig. 6a). Furthermore, the zoning in the ferroan calcite is also highlighted by carbonate staining, colouring the calcite to purple and then blue towards the centre of the pore indicating varying Fe content (Fig. 5d; Appendix Cc). The calcite spars show a rather patchy occurrence. Framework grains, especially quartz grains are corroded by the ferroan sparry calcite, showing pitted margins and embayments (Fig. 5a; Appendix Cg), and volcanic rock fragments are partially replaced by ferroan calcite. Furthermore, the ferroan spar engulfs overgrowths of quartz crystals (Appendix Ce). Ferroan calcite also

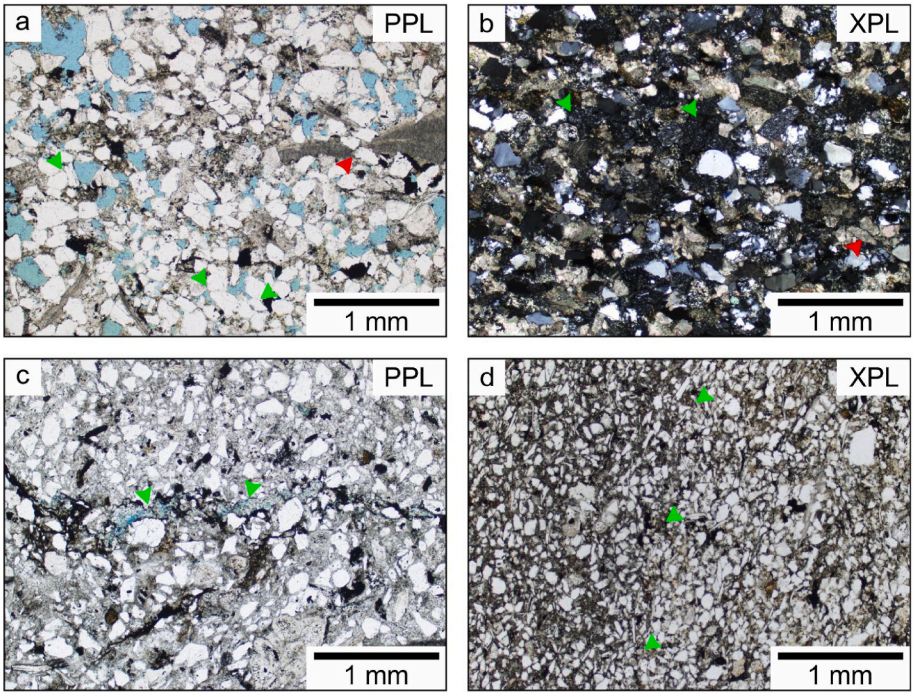

Fig. 4. Petrographic and textural features of arenites and wackes. a) Texture of an arenite in plane-polarized light (PPL; W–1; 2462.1 m MD), showing oversized pores, filled with blue epoxy, and the tangential to long and concavo-convex contacts between framework grains (green arrows), as well as fossil fragments separated by quartz grains (red arrow). b) Texture of an arenite in cross-polarized light (XPL; W–14; 2182.0 m MD). Framework grains include quartz grains, volcanic (green arrows) and carbonate (red arrow) rock fragments. c) Texture of a wacke (W–1; 2461.8 m MD). Framework grains float in the calcareous matrix and a dissolution pore cross-cut the section along with a micro-stylolite (green arrow). d) Microphotograph showing the transition (green arrows) from wacke to arenite (W–14; 2109.0 m MD) as indicated by the decrease in the proportion of the matrix from left to right. (For interpretation of the references to colour in this figure legend, the reader is referred to the Web version of this article.)

preserves embayments that are partially filled with kaolinite (Appendix Cf), but the fracture-filling calcite grows over kaolinite (Fig. 5e). The skeletal grains are highlighted by micritic envelopes. Most preserved bioclasts stained purple or blue while brachiopod fragments stained pink (Fig. 5f; Appendix Cc).

4.2.2.2. Dolomite. Dolomite forms finely crystalline (30–70 μm) planar subhedral-to-euhedral (*Dol1*), as well as medium-crystalline (up to 250 μm) nonplanar textures (*Dol2*; Fig. 6). The latter is occasionally characterised by curved crystal faces. Regardless of texture, the dolomite crystals locally show a brownish colouration in transmitted light (Fig. 6b), especially around the cleavage planes and outer rims. The brown colouration of dolomite is common where the crystals are associated with pyrite. All dolomites are non-cathodoluminescent (Fig. 6c and d). Locally, the dolomite may display zonation under UV and blue-light irradiation (Fig. 6a). The edges of the planar and nonplanar dolomite are stained turquoise, whereas the entirety of the nonplanar crystals stain turquoise was also observed (Fig. 6e; Appendix Cd). The planar dolomite crystals contain a rim of fluid inclusions in the otherwise inclusion-poor crystals. Furthermore, less typically, spots of ferroan calcite and framboidal to euhedral pyrite also occur within the planar dolomite (Fig. 6c, f). The planar dolomite occludes primary and secondary pores, is partially engulfed by calcite, pyrite, kaolinite and quartz crystals (Figs. 6 and 7; Appendix Cf and De, h) and also appears as a replacive phase scattered throughout the samples. The nonplanar dolomite crystals either fill intergranular pores or clog the chambers of preserved fossils (Fig. 6d; Appendix Dc).

4.2.2.3. Quartz. Quartz cement occurs as syntaxial overgrowth, outgrowth (Fig. 7a) and it heals microfractures in detrital quartz grains. Quartz cement is less common in calcite cemented samples. Over- and outgrowths partially or completely occlude the intergranular pores in sandstones and siltstones. The overgrowths form up to 100 μm-wide rims around the quartz grains. Moreover, up to 200-μm-sized outgrowths are also present in some samples. The authigenic quartz is non-cathodoluminescent. Large overgrowths engulf authigenic dolomite rhombs (Fig. 7a). A thin coat of clay minerals and iron oxyhydroxides cover the crystal facets (Fig. 7b; Appendix Dg, h) and locally highlight the boundaries between quartz grains in densely packed lithologies.

4.2.2.4. Illite. Illite flakes and filaments occur in the samples as mineral coatings (Fig. 7b), covering the authigenic quartz and kaolin group minerals. Illite shows black and brown colouration in transmitted light.

4.2.2.5. Kaolin minerals. Individual kaolin crystals are less than 2-μm-thick and form vermicular aggregates (Fig. 8a). The stacked booklets of pseudohexagonal crystals are up to 40-μm-thick. Besides the vermiform kaolin, up to 6-μm-thick blocky crystals are also present in the samples and preserve the original stacking pattern (Fig. 8a). Kaolin is white or shows brownish to blackish colouration in transmitted light, and a bright, deep blue CL (Fig. 6c, f). Booklet-like piles of kaolin are locally associated with muscovite and fill the space between split flakes (Fig. 8b). Kaolin piles are also linked to intragranular pores of feldspar grains or argillaceous rock fragments (Fig. 8c and d). Furthermore, the stacked booklets also clog the chambers of fossils (Fig. 8e). More commonly, vermicular kaolin exists in between framework grains, occluding intergranular and oversized pores completely or partially. Moreover, kaolin also sits on the wall of ferroan calcite (Appendix Cf) and calcite-filled fractures (Fig. 5e). Occasionally, neoform kaolin is present in the embayments of detrital quartz grains. Kaolin crystals surround pyrite framboids and dolomite rhombs (Fig. 6f), or it is engulfed by quartz overgrowth, outgrowth (Fig. 8f) and ferroan calcite (Fig. 5e). Kaolin crystals are densely stacked in association with argillaceous debris squeezed into rigid framework grains (Fig. 8c and d).

4.2.2.6. Pyrite. Pyrite occurs as framboidal aggregates, sized up to 50 μm, and locally mm-sized single crystals or nodules made up of anhedral-to-euhedral crystals. Spherical aggregates are either associated with bioclasts (Fig. 9a), develop within chambers pre-dating calcite, or replace skeletal grains, forming ghosts after the original fossils. Furthermore, framboids occur between the framework grains, appear floating in the calcareous matrix (Fig. 9b) or sit on the edge of detrital grains. The subhedral-to-euhedral crystals are common along dissolution seams together with solid bitumen (Fig. 9c), and form rims and nodules along framework grains, especially quartz grains (Fig. 9d) and lithic fragments, and accessory minerals such as rutile. Pyrite crystals

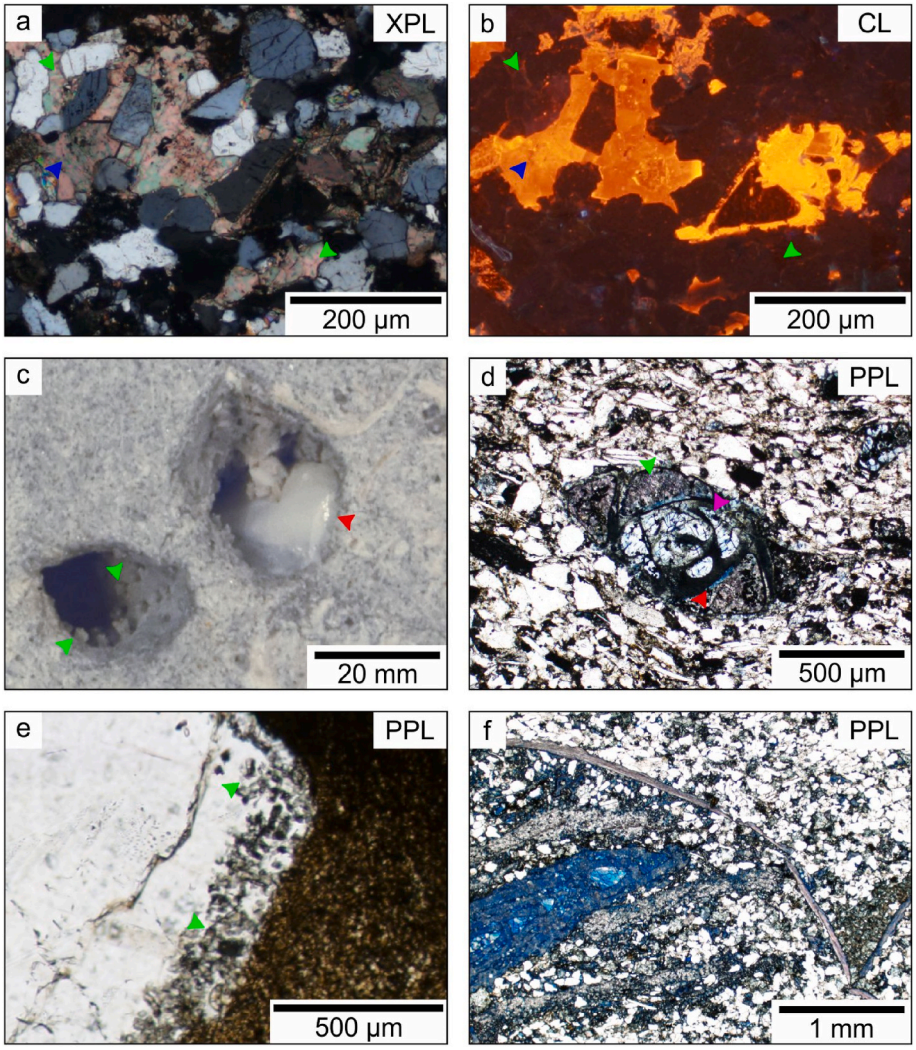

Fig. 5. Photomicrographs of calcite cement. a) and b) Poikilotopic calcite cemented arenite (W–9; 2811.0 m MD). Green arrows point to non-luminescing calcite, whereas the blue arrow marks an orange luminescent one. c) Single coarse crystal (red arrow) partially fills a moldic pore and calcite crystals (green arrows) sit in equidistance on the wall of a moldic pore (W–1; 2459.9 m MD). d) The outer chambers of a miliolid foraminifer are filled by purple-stained calcite (green arrow), which embays pyrite framboids. Towards the central chamber, which is clogged by non-ferroan dolomite (pink arrow), a rim of blue-stained calcite is also present along the margin of dolomite (red arrow; W–1; 2603.4 m MD). e) Fracture-filling coarse-crystalline calcite with well-developed crystal facets embays kaolinite (green arrows; W–15; 2350.5 m MD). f) Pink-stained bioclast fragments (brachiopods) and blue-stained skeletal grain (nummulite) in an arenite (W–15; 2354.5 m MD). (For interpretation of the references to colour in this figure legend, the reader is referred to the Web version of this article.)

consume dolomite (Appendix Dh) and less typically occur as inclusions in planar dolomite rhombs (Fig. 6f). Pyrite is locally surrounded by brownish iron oxyhydroxide phases (Fig. 6b, f), which typically also cover framework grains.

4.2.3. Porosity

Blue epoxy impregnated thin sections reveal that the partial or complete dissolution of detrital intra- and extrabasinal grains control the intergranular and intragranular porosity (Fig. 4a; Appendix Da, e and f). Moldic pores are also present preserving the shape of the fossil fragments (Fig. 5c; Appendix Ad). The size of the pores is typically more than two times greater than the diameter of the framework grains. These oversized pores ensure the interconnectedness of pores throughout the sandstones regardless of the abundance of the matrix. Authigenic minerals, such as ferroan calcite and kaolin crystals, and dolomite often occlude the pores but intercrystalline pores between the cement crystals remain (Fig. 6f). Fracture porosity also exists either as open or partially healed fractures. The outlined hybrid porosity varies even at the microscale and shows considerable heterogeneity in the spatial characteristics of the pore system. Even though the porosity of sandstones is dominated by secondary porosity, primary porosity is also preserved, such as intraskeletal pores.

4.3. Fluid inclusion petrography and microthermometry

Representative samples, including centimetre-sized euhedral calcite in an oversized pore, centimetre-thick fracture-filling calcite, as well as samples of arenite, wacke, siltstone and drill cuttings were selected for detailed FI study. These samples contain authigenic minerals, such as calcite, dolomite and quartz that host numerous FIs of suitable size. The results of the FI studies are summarized in Table 3.

4.3.1. Calcite

Numerous FIs are present in the various bright to dull orange-luminescing ferroan calcite crystals, including euhedral calcite (Cal_{EU}) that fills oversized pores, equant calcite spar that fills the chambers of preserved bioclasts or intragranular pore spaces (Cal_{EQ}), and fracture-filling calcite (Cal_{FF}).

4.3.1.1. Euhedral calcite (Cal_{EU}). The euhedral calcite hosts primary FIs, forming planes along crystal-growth zones. The FIs are sized up to 50 μm and have shapes of negative crystal and rounded forms as well. The inclusions are colourless and non-fluorescent two-phase ($L_{aq} + V$) with $\varphi_V \approx 0.1–0.2$ at room temperature and are interpreted as primary aqueous inclusions (AIs). Raman microspectroscopy indicates the presence of gaseous hydrocarbons, methane and ethane, in the vapour phase of some AIs (Fig. 10). The homogenisation occurs into the liquid phase ($L_{aq} + V \rightarrow L_{aq}$), the T_h varies in a narrow range from 129 °C to 137 °C (n = 85; Fig. 11). The T_m(Ice) ranges between −3.4 °C and −2.5 °C (n = 85; Fig. 12), indicating a range of salinity between 4.2 mass% and 5.6 mass % NaCl equivalent. No visual changes were observed in AIs while cooling them to −160 °C, indicating the lack of a clathrate phase.

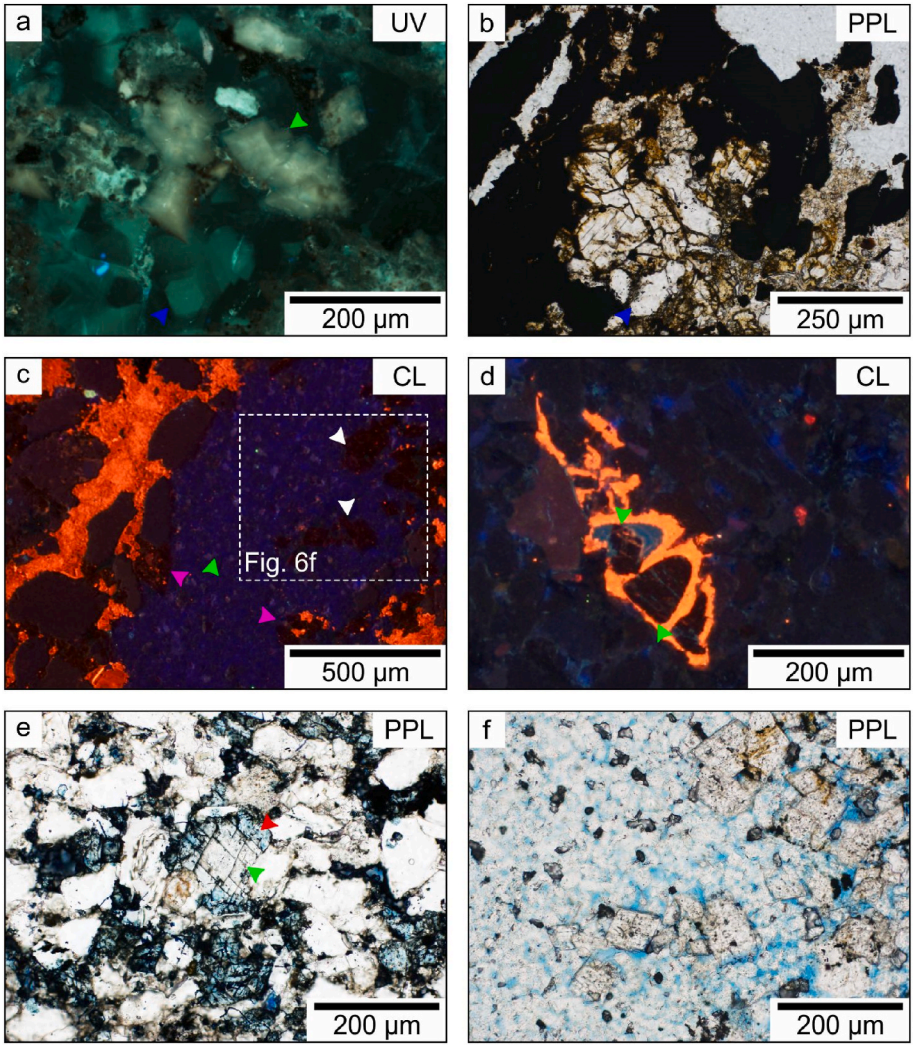

Fig. 6. Photomicrographs of dolomite phases. a) Zoned dolomite (green arrow) and calcite (blue arrow) under UV-light irradiation (W–15; 2358.0 m MD). b) Medium-crystalline non-planar dolomite crystals surrounded by opaque minerals and solid bitumen. Dolomite shows brown colouration along cleavage planes (W–7; 2460.2 m MD). c) Blue-luminescing kaolinite (green arrow) and non-luminescent dolomite (pink and white arrows) fill an oversized pore. Orange-luminescing calcite replaces non-luminescent detrital quartz grains. Non-luminescent dolomite partially replaces luminescing calcite (pink arrow; W–1; 2455.3 m MD). d) Orange-luminescing skeletal grain is filled by non-luminescent dolomite (green arrow; W–9; 2810.5 m MD). e) Turquois-stained ferroan dolomite (red arrow) grows over non-stained planar euhedral dolomite rhomb (green arrow; W–15; 2354.5 m MD). f) Planar euhedral-subhedral dolomite rhombs embayed by kaolinite. Dolomite hosts subhedral pyrite crystals and shows brownish colouration (W–1; 2455.3 m MD). (For interpretation of the references to colour in this figure legend, the reader is referred to the Web version of this article.)

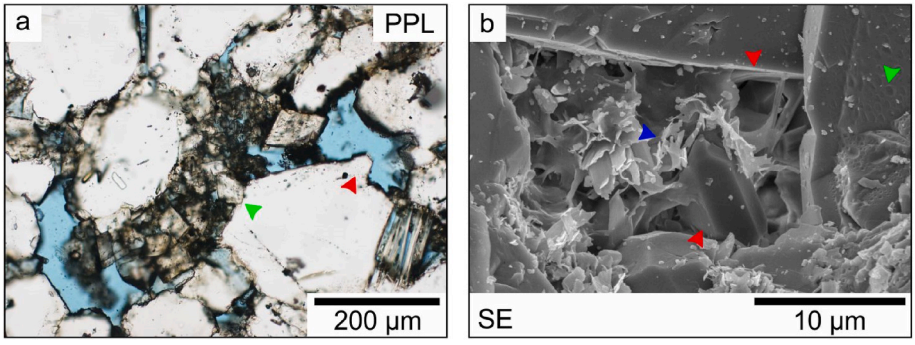

Fig. 7. Photomicrographs of quartz cement. a) Quartz cement forms syntaxial overgrowths and outgrowths (red arrow) pointing towards pores, filled with blue epoxy. Planar euhedral dolomite rhomb (green arrow) abuts against quartz overgrowth (W–1; 2455.3 m MD). b) Illite flakes (blue arrow) cover euhedral quartz crystals (red arrows) in a secondary electron image (SE). Dissolution pits are marked by green arrows (W–9; 2809.5 m MD). (For interpretation of the references to colour in this figure legend, the reader is referred to the Web version of this article.)

4.3.1.2. Equant calcite (Cal_{EQ}). The inclusions form groups either in the core of the equant sparry calcite or are present throughout the entire calcite crystal, which argues for primary origin. The inclusions are sized up to 11 µm and contain colourless liquid and vapour phases with $\varphi_V \approx$ 0.1–0.2 at room temperature. The FIs are non-fluorescent and are defined as aqueous inclusions. The fluids homogenise into the liquid phase ($L_{aq} + V \rightarrow L_{aq}$) with T_h varying between 126 °C and 141 °C (n = 35; Fig. 11). The T_m(Ice) ranges between −3.1 °C and −2.8 °C (n = 17; Fig. 12), indicating a range of salinity between 4.7 mass% and 5.1 mass % NaCl equivalent. A decrease in T_h across a single spar towards the edge is apparent in these FIAs, but the values of T_m(Ice) do not show similar variation.

Secondary FIAs are also present in the equant sparry calcite. FIs form trails and crosscut several calcite crystals. The FIs are up to 10 µm in size, are colourless in plane-polarized light, and have a yellowish-orange fluorescence in UV-light irradiation (Fig. 13). Groups of fluorescent FIs, containing a maximum of five inclusions, also exist in these spars with a maximum FI size of 10 µm. These inclusions are interpreted as HCFIs and are two-phase inclusions ($L_{hc} + V$; $\varphi_V \approx$ 0.1–0.2) and homogenise into the liquid phase ($L_{hc} + V \rightarrow L_{hc}$) between 105 °C and 142 °C (n = 37; Fig. 11). Two-phase, colourless aqueous FIs of up to 5 µm size ($L_{aq} + V$; $\varphi_V \approx 0.2$) also occur within these FIAs. These aqueous FIs

Table 2
The occurrence of the diagenetic minerals in the investigated lithotypes.

	Conglomerate	Arenite	Wacke		Siltstone
			Argillaceous matrix	Calcareous matrix	
Calcite					
spar	✓	✓	✓	✓	✓
fracture-filling	✓	✓	✓	✓	✓
Dolomite					
rhomb		✓	✓		
pore-filling saddle-like		✓	✓		✓
Quartz					
overgrowth/outgrowth		✓	✓		
pore-filling	✓	✓	✓		✓
Illite		✓	✓	✓	✓
Kaolin minerals	✓	✓	✓		✓
Pyrite					
framboidal		✓	✓	✓	✓
euhedral		✓	✓		

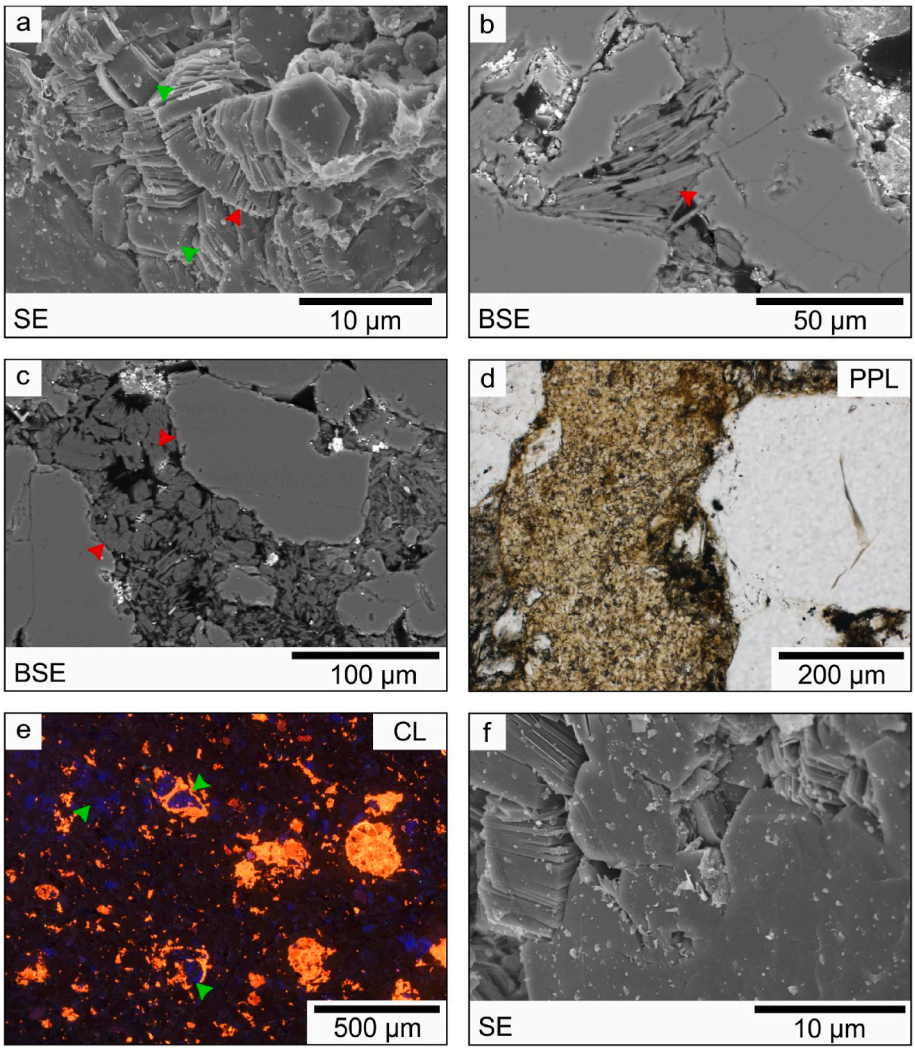

Fig. 8. Photomicrographs of kaolin cement. a) Stacked booklets of pseudohexagonal kaolin crystals. The red arrow points to a less than 2-µm-thick crystal, whereas the green arrows mark the thicker blocky crystals (W–9; 2810.0 m MD). b) Backscattered electron (BSE) image of booklet-like piles of kaolin (red arrow) that are associated with muscovite and fill the space between split flakes (W–1; 2455.3 m MD). c) Kaolin crystals (red arrows) replacing framework grain (W–1; 2455.3 m MD). d) Densely stacked kaolin in association with argillaceous debris squeezed into rigid framework grains (W–7; 2460.2 m MD). e) Blue-luminescing kaolinite (green arrows) fills chambers of orange-luminescing fossils and forms nest in intergranular pores (W–14; 2109.0 m MD). f) Syntaxial quartz overgrowths embay kaolin crystals (W–9; 2810.0 m MD). (For interpretation of the references to colour in this figure legend, the reader is referred to the Web version of this article.)

homogenise into the liquid phase ($L_{aq} + V \rightarrow L_{aq}$), and the T_h varies from 115 °C to 146 °C (n = 16; Fig. 11). The T_m(Ice) ranges between −5.2 °C and −1.6 °C (n = 16; Fig. 12), indicating a range of salinity between 2.7 mass% and 8.1 mass% NaCl equivalent. The intense fluorescence of the co-occurring HCFIs prevented the application of Raman microspectroscopy to determine the gaseous hydrocarbons in the vapour phase.

4.3.1.3. Fracture-filling calcite (Cal_{FF}). Fracture-filling blocky calcite hosts FIs that form planes along growth zones. The primary FIs are up to 25 µm in size and are characterised by rounded and negative crystal shapes. The inclusions are colourless in plane-polarized light and show bluish epifluorescence (Fig. 13). The HCFIs are two-phase ($L_{hc} + V$) with $\varphi_V \approx 0.1$–0.2 at room temperature. These inclusions homogenise to the liquid phase ($L_{hc} + V \rightarrow L_{hc}$) between 103 °C and 123 °C (n = 27; Fig. 11). No visual changes were observed in HCFIs while cooling them

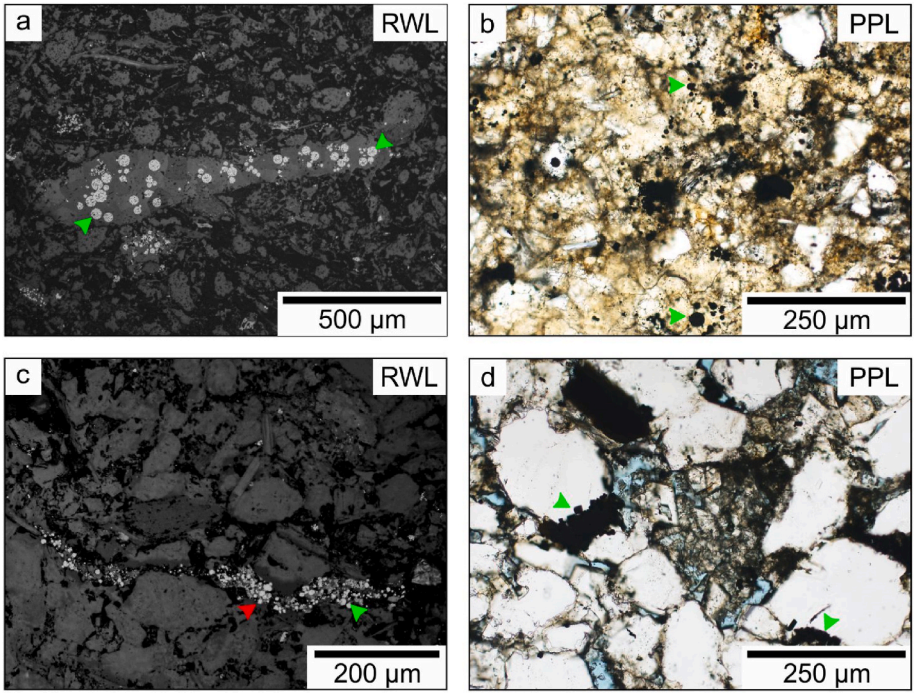

Fig. 9. Photomicrographs of authigenic pyrite. a) Pyrite framboids (green arrows) sit within a fossil in reflected white light (RWL; W–1; 2603.1 m MD). b) Pyrite framboids (green arrows) engulfed by calcite spars in a wacke (W–1; 2461.8 m MD). c) Pyrite crystals (green arrow) associated with micro-stylolite (red arrow; W–1; 2504.0 m MD). d) Euhedral pyrite crystal aggregates (green arrows) replacing quartz grains (W–1; 2455.3 m MD). (For interpretation of the references to colour in this figure legend, the reader is referred to the Web version of this article.)

Table 3
Petrographic and microthermometric characteristics of the studied FIAs.

Mineral phase	Genetic origin	Size [µm]	Colour in transmitted light	Colour under UV-light irradiation	Composition	Vapour phase ratio	Homogenisation process	T_h [°C]	T_m(Ice) [°C]	salinity [mass %]
Cal_{EU}	primary	<50	colourless	non-fluorescent	$L_{aq} + V$	$\varphi_V \approx 0.1–0.2$	$L_{aq} + V \rightarrow L_{aq}$	129–137	−3.4 to −2.5	4.2–5.6
Cal_{EQ}	primary	<11	colourless	non-fluorescent	$L_{aq} + V$	$\varphi_V \approx 0.1–0.2$	$L_{aq} + V \rightarrow L_{aq}$	126–141	−3.1 to −2.8	4.7–5.1
	secondary	<10	colourless	non-fluorescent	$L_{aq} + V$	$\varphi_V \approx 0.2$	$L_{aq} + V \rightarrow L_{aq}$	115–146	−5.2 to −1.6	2.7–8.1
		<5	colourless	yellowish-orange	$L_{hc} + V$	$\varphi_V \approx 0.1–0.2$	$L_{hc} + V \rightarrow L_{hc}$	105–142		
Cal_{FF}	primary	<25	colourless	non-fluorescent	$L_{aq} + V$	$\varphi_V \approx 0.2$	$L_{aq} + V \rightarrow L_{aq}$	105–126	−2.1 to −1.3	2.2–3.6
		<13	colourless	bluish	$L_{hc} + V$	$\varphi_V \approx 0.1–0.2$	$L_{hc} + V \rightarrow L_{hc}$	103–123		
Dol	primary	<19	colourless	non-fluorescent	$L_{aq} + V$	$\varphi_V \approx 0.2–0.3$	$L_{aq} + V \rightarrow L_{aq}$	105–142	−5.5 to −0.6	1.2–8.5
Qtz	primary	<17	colourless	non-fluorescent	$L_{aq} + V$	$\varphi_V \approx 0.2–0.3$	$L_{aq} + V \rightarrow L_{aq}$	110–136	−3.4 to −1.5	2.6–5.6
	secondary	<10	colourless	non-fluorescent	$L_{aq} + V$	$\varphi_V \approx 0.2$	$L_{aq} + V \rightarrow L_{aq}$	120–129	−2.2 to −0.9	1.6–3.7
		<5	colourless	bluish-green	$L_{hc} + V$ $L_{aq} + L_{hc} + V$ $L_{hc} + V + S_{bit}$	$\varphi_V \approx 0.1–0.2$ $\varphi_S \approx 0.1–0.2$	$L_{hc} + V \rightarrow L_{hc}$ $L_{hc} + V + S_{bit} \rightarrow L_{hc} + S_{bit}$	117–130		

Cal_{EU} – euhedral calcite, Cal_{EQ} – equant sparry calcite, Cal_{FF} – fracture-filling calcite, Dol – planar dolomite, Qtz – quartz.

to −160 °C. Cogenetic colourless two-phase AIs ($L_{aq} + V$; $\varphi_V \approx 0.2$), with a maximum of 13 µm diameter, are also present in FIAs. Raman microspectroscopy of the aqueous FIs was hindered because of the intense fluorescence of the HCFIs. The homogenisation occurs in the liquid phase ($L_{aq} + V \rightarrow L_{aq}$) and the T_h varies from 105 °C to 126 °C (n = 16; Fig. 11). The T_m(Ice) ranges between −2.1 °C and −1.3 °C (n = 16; Fig. 12), indicating a range of salinity between 2.2 mass% and 3.6 mass % NaCl equivalent.

4.3.2. Dolomite

Planar subhedral-to-euhedral rhombs (*Dol1*) in the sandstones contain FIs. Primary FIAs developed across the crystal outwards from the core. The FIs are sized up to 19 µm and are generally characterised by negative crystal shapes. At room temperature, in plane-polarized light, the inclusions consist of colourless liquid and vapour phase ($L_{aq} + V$; $\varphi_V \approx 0.2–0.3$). The primary FIs homogenised in the liquid phase ($L_{aq} + V \rightarrow L_{aq}$) and T_h values fall between 105 °C and 142 °C (n = 43; Fig. 11). The T_m(Ice) varies from −5.5 °C to −0.6 °C (n = 30; Fig. 12), indicating a rather broad salinity range between 1.2 mass% and 8.5 mass % NaCl equivalent. The distribution of the T_h and T_m(Ice) display a distinct spatial trend in these FIAs (Fig. 12): the T_h decreases from a maximum of 142 °C in the core to a minimum of 106 °C towards the rim of the crystal, whereas the T_m(Ice) increases from a minimum of −5.5 °C in the core to a maximum of −2.2 °C towards the edge.

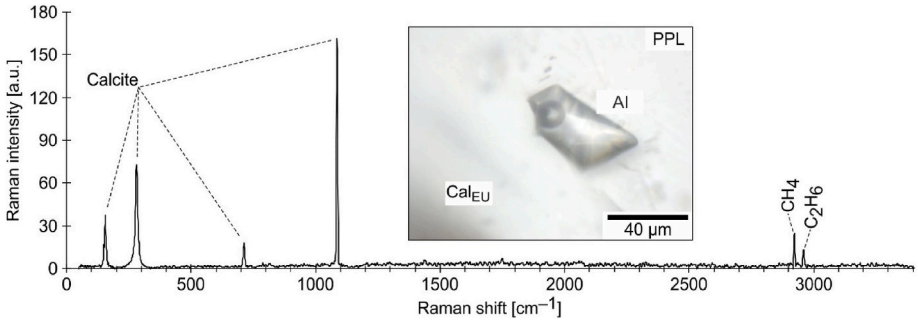

Fig. 10. Representative Raman spectrum of the vapour phase within an aqueous inclusion (AI) assemblage of euhedral calcite (Cal_{EU}).

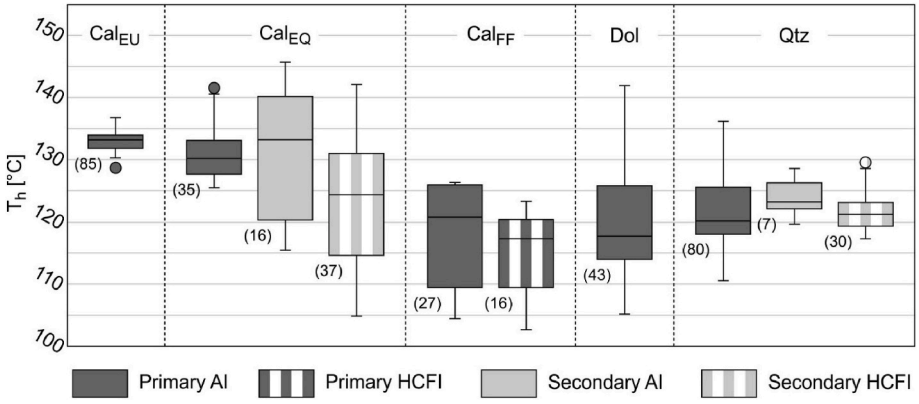

Fig. 11. Box-plot of the homogenisation temperatures (T_h). The numbers in brackets correspond to the number of analysed FIs. Cal_{EU} – euhedral calcite, Cal_{EQ} – equant calcite, Cal_{FF} – fracture-filling calcite, Dol – planar dolomite, Qtz – quartz.

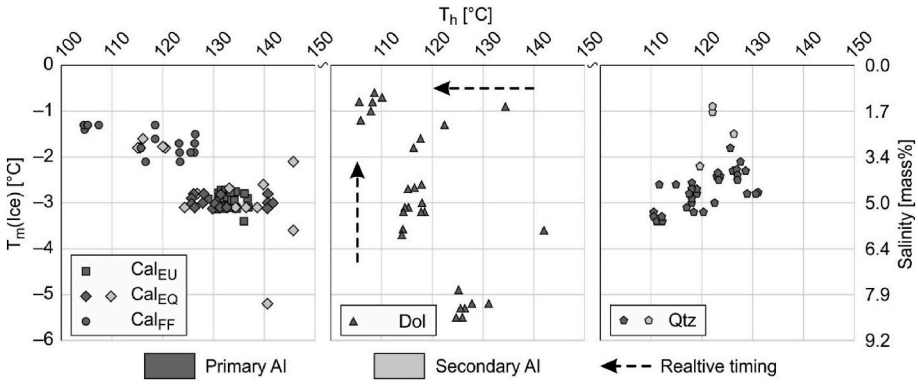

Fig. 12. Cross-plot of homogenisation temperatures (T_h) vs. final ice melting temperatures (T_m(Ice)) of the analysed aqueous fluid inclusion assemblages. Arrows, representing the relative timing of FI entrapments, point to younger FIs. Cal_{EU} – euhedral calcite, Cal_{EQ} – equant calcite, Cal_{FF} – fracture-filling calcite, Dol – planar dolomite, Qtz – quartz.

4.3.3. Quartz

Authigenic quartz occurs as syntaxial overgrowth, outgrowth and as healed microfractures in detrital quartz grains in the sandstones and siltstones. Fluid inclusion assemblages occur along the dust rims in overgrowths, forming groups in pore-filling quartz and along with healed microfractures.

Primary FIAs along the dust rims are sized up to 17 µm and their shapes vary among negative crystal shaped, rounded and amoeboid forms. These inclusions are liquid dominant ($\varphi_V \approx 0.2–0.3$) and contain non-fluorescent, colourless fluid and vapour phases ($L_{aq} + V$). The homogenisation occurs into the liquid phase ($L_{aq} + V \rightarrow L_{aq}$) with T_h varying from 110 °C to 136 °C (n = 80; Fig. 12). The T_m(Ice) ranges between −3.4 °C and −1.5 °C (n = 38; Fig. 13), indicating a range of salinity between 2.6 mass% and 5.6 mass% NaCl equivalent.

Secondary FIAs fluoresce intensely with bluish-green colour under UV epi-illumination (Fig. 14) and are interpreted as HCFIs. The HCFIs are either colourless or brownish in transmitted light regardless of fluorescence colour. The inclusions are characterised by rounded and irregular shapes and range in size up to 10 µm. The HCFIs are dominantly two-phase ($L_{hc} + V$; $\varphi_V \approx 0.1–0.2$) inclusions. Locally one-phase (L_{hc}) and three-phase ($L_{aq} + L_{hc} + V$) HCFIs are also present. Occasionally brownish black to opaque solid bitumen occurs in some ($L_{hc} + V + S_{bit}$) HCFIs. The volume fraction of the bitumen phase varies in a wide range ($\varphi_S \approx 0.01–0.2$) and is interpreted as an accidently captured phase. Phase transition of the bitumen did not occur upon heating to 200 °C. Similarly, no visual changes occurred in HCFIs while cooling

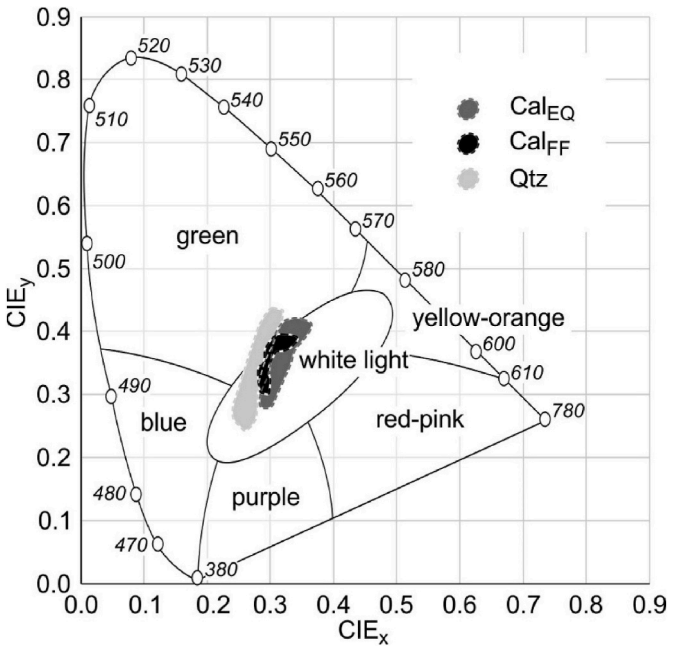

Fig. 13. Fluorescence colours of the hydrocarbon-bearing inclusions plotted on a CIE-1931 diagram (Smith and Guild, 1931) for visual comparison. Numbers presented along the colour envelope correspond to wavelengths in nanometres.

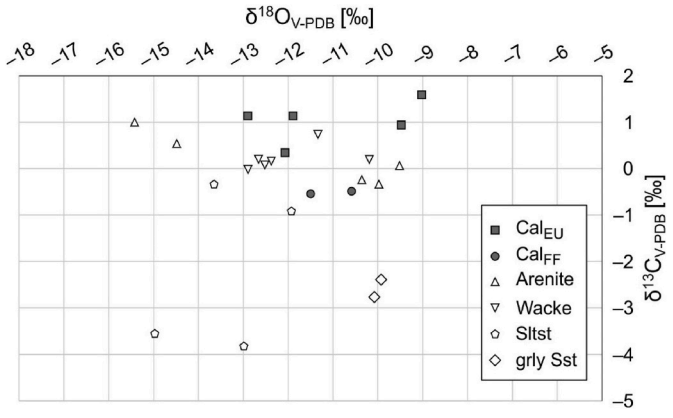

Fig. 14. Cross-plot of the stable carbon ($\delta^{13}C$) and oxygen ($\delta^{18}O$) isotope compositions of the investigated samples. Cal_{EU} – euhedral calcite, Cal_{FF} – fracture-filling calcite, Sltst – siltstone, grly Sst – sandstone with gravel.

them to −160 °C. The two-phase inclusions undergo homogenisation to the liquid phase ($L_{hc} + V \rightarrow L_{hc}$) and the T_h of HCFIs is between 117 °C and 130 °C (n = 28; Fig. 12). The three-phase HCFIs homogenise to two-phase inclusions ($L_{hc} + V + S_{bit} \rightarrow L_{hc} + S_{bit}$) and the T_h ranges from 119 °C to 121 °C (n = 2; Fig. 12). Spatially rare cogenetic, up to 7 μm-diameter, two-phase colourless aqueous FIs ($L_{aq} + V$; $\varphi_V \approx 0.2$) also occur within these FIAs. The aqueous FIs homogenise into liquid phase ($L_{aq} + V \rightarrow L_{aq}$) and the T_h varies from 120 °C to 129 °C (n = 7; Fig. 12). The T_m(Ice) ranges between −2.2 °C and −0.9 °C (n = 4; Fig. 13), indicating a range of salinity between 1.6 mass% and 3.7 mass% NaCl equivalent.

4.4. Stable carbon and oxygen isotope compositions

The stable carbon and oxygen isotope compositions of the investigated samples are listed in Table 4. The $\delta^{13}C$ and $\delta^{18}O$ values of the euhedral calcite vary from 0.34‰ to 1.61‰ and from −12.90‰ to −11.89‰, respectively. The fracture-filling calcite is characterised by

Table 4
The stable carbon ($\delta^{13}C$) and oxygen ($\delta^{18}O$) isotope compositions of the investigated samples.

Sample type	Carbonate cement phase	$\delta^{13}C$	$\delta^{18}O$
		[‰; V-PDB]	
Wacke	Fe-Cal with	0.16	−12.38
	Dol1	0.20	−10.19
		0.20	−12.66
		0.74	−11.34
		0.08	−12.52
		−0.02	−12.90
Arenite	Fe-Cal with	0.06	−9.52
	Dol1	1.00	−15.42
		0.54	−14.48
	Fe-Cal and	−0.34	−9.98
	Dol2	−0.24	−10.36
Sandstone with	Fe-Cal and	−2.77	−10.08
gravel	Dol1/Dol2	−2.39	−9.93
Siltstone	Fe-Cal with	−3.56	−14.98
	Dol1/Dol2	−3.83	−12.99
Calcite	Euhedral	1.61	−12.18
		1.13	−12.90
		0.34	−12.07
		1.13	−11.89
		0.94	−12.67
	Fracture-filling	−0.54	−11.50
		−0.49	−10.59

Fe-Cal – ferroan calcite, Dol1 – planar dolomite, Dol2 – nonplanar dolomite.

−0.54‰ to −0.49‰ for $\delta^{13}C$, and −11.50‰ to −10.59‰ for $\delta^{18}O$ values. The $\delta^{13}C$ of the bulk rock samples is between −3.83‰ and 1.00‰, and the $\delta^{18}O$ ranges from −15.42‰ to −9.52‰ (Fig. 14).

5. Discussion

The paragenetic sequence was reconstructed based on textural relationships between diagenetic minerals, as well as fluid inclusion and stable carbon and oxygen isotope data. The paragenesis is summarized in Fig. 15 and the processes are explained in the following sections.

5.1. Control of depositional environment on early diagenetic processes

The Eocene sedimentary sequence in the study area records the transition from a continental to a lagoonal depositional environment (Gidai, 1978; Less, 2005), recording the first signs of the Priabonian transgression (Báldi and Báldi-Beke, 1985), which process fundamentally controls the fabric, texture, as well as the initial porosity and permeability of the accumulating sediments. The coal-bearing upper part of the Kosd Formation accumulated in a marine delta and is intercalated with sandstone and siltstone (Fig. 2), containing miliolid foraminifers (Körmös et al., 2020), indicating low-energy environments with varying sea-level. The Kosd Formation is followed by the shelf deposits of the biogenic Szépvölgy Limestone Formation (Kázmér, 1985), which occurs in the NE part of the study area, in the Well–15 (Fig. 2b), suggesting a continuous basin development. Even though the biogenic Szépvölgy carbonate is not present in the SW part of the study area, the preserved bioclasts (Figs. 4a and 5d, f, 6d, 8e, 9a; Appendix Cc) in the studied sandstones are marine benthic (e.g., nummulites and miliolid foraminifers), sessile, attached (e.g., brachiopods), filter-feeding (e.g., bryozoans), grazer or burrower (e.g., echinoids) organisms and indicate photic zone (e.g., red algae) of the water column in a sandy shelf area (cf.,Scholle and Ulmer-Scholle, 2003). Sediments rich in intra-basinal carbonate grains (e.g., bioclasts) are prone to exhaustive carbonate cementation, reducing the initial depositional porosity and permeability.

The mineralogical composition of the rock components is a fundamentally important control on what mineralogical and chemical reactions play out during diagenesis. In clastic rocks, the tectonostratigraphy, i.e., the hinterland determines the source of the

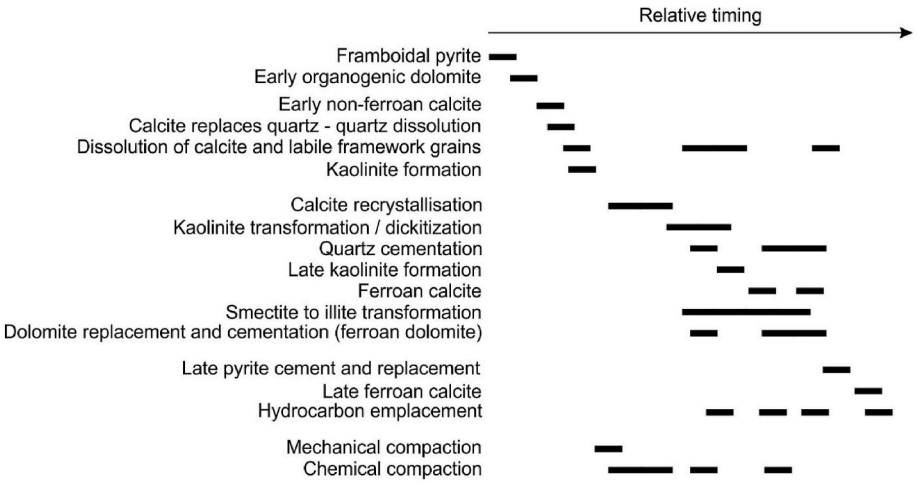

Fig. 15. Reconstructed paragenetic sequence of the south-central part of Hungarian Palaeogene Basin.

detrital material. From the Late Cretaceous, the regional orogenic uplift led to subaerial exposure of the Mesozoic strata, including sedimentary and magmatic sequences, abundant in feldspar (e.g., Szarvaskő-Mónosbél Nappe in the Bükk Unit), and as a consequence, significant denudation occurred (Less, 2005; Haas and Kovács, 2012). The gradual north-eastward trending of the Eocene transgression reached the study area during the Bartonian and Priabonian (Báldi and Báldi-Beke, 1985; Báldi-Beke, 2003a, 2003b), allowing the accumulation of sediments with varying feldspar content. The widespread occurrence of kaolinite on the erosional surfaces in the hinterland (Viczián, 1987, 1995) and the stacked booklets, clogging the chambers of fossils (Fig. 8e) emphasize the importance of chemical weathering of a feldspar-bearing source that resulted in the accumulation of detrital kaolin minerals.

5.2. Bacterial sulphate reduction and organogenic dolomite

The presence of densely packed framboidal pyrite aggregates within the chamber of bioclasts and around their test (Fig. 9a) indicates locally reducing conditions during formation due to the oxidation of organic matter that was incorporated within skeletal structures. Moreover, the framboids, floating in the calcareous matrix (microspar; Fig. 9b) suggest the presence of sulphate-rich marine pore waters, the availability of reactive iron and the activity of sulphate-reducing bacteria (Sweeney and Kaplan, 1973; Gong et al., 2008). In some cases, planar dolomite rhombs enclose pyrite framboids, which may imply the localised occurrence of organogenic dolomite formation (Baker and Kastner, 1981; Morad et al., 2000). Organogenic dolomite is typically very finely crystalline and is interpreted to form when marine and meteoric waters mix and the sulphate ions are removed by the bacterial reduction in the bacterial sulphate-reducing zone (Petrash et al., 2017). However, the larger sizes of the dolomite rhombs in this study together with the >100 °C homogenisation temperatures suggest that, if present, organogenic dolomite only served as nucleation sites for the later, high-temperature ones. Bacterial sulphate reduction and the formation of potentially organogenic dolomite nuclei are interpreted to have taken place in a marine palaeoenvironment.

5.3. Origin of the microspar matrix

The high volume occupied by intergranular calcareous matrix (microspar) in the wackes (Fig. 4c), the absence of authigenic minerals other than those formed in the bacterial sulphate-reduction zone, and the lack of framework grain rearrangement features indicate an early, near-surface origin of the microspar, likely as intergranular micrite matrix that underwent crystal enlargement (cf., Bathurst, 1975). The ferroan character of the microspar may indicate suboxic conditions in the bottom waters but the values of $\delta^{13}C$ (−0.02 to +0.74; Table 4) and the preserved bioclast assemblage argue for a precursor carbonate mud that accumulated in well-oxygenated water (Morad, 1998). Furthermore, under suboxic conditions, the available ferrous iron is typically incorporated into minerals, such as pyrite, in the bacterial sulphate-reduction zone. Nevertheless, the later precipitated calcite below the sediment-water interface may locally show ferroan character but it is generally Fe-poor. The ferroan nature of the calcite is thus more likely the result of recrystallisation (neomorphism) in a subsequent diagenetic phase.

5.4. Early kaolinization

Dissolution and alteration of silicates, especially the kaolinization of feldspar and mica (Fig. 8b and c) are common processes in the presence of low ionic strength meteoric waters (Worden and Burley, 2003). In shallow marine environments, the shelf is exposed to the freshwater influx and meteoric recharge during sea-level lowstand (Worden and Morad, 2003 and references therein). The $\delta^{18}O$ values of the wackes (avg.: −12.0‰ V-PDB; Table 4) support the presence of meteoric or mixed marine-meteoric pore water during calcite precipitation. Assuming 30 °C surface ocean temperature (Tindall et al., 2010) during early calcite formation, the calcite-water oxygen isotope fractionation equation (O'Neil et al., 1969) reveals a porewater characterised by an average $\delta^{18}O_{V\text{-}SMOW}$-value of −8.3‰. Considering the negligible land-covering ice-volume during the Palaeogene, and the $\delta^{18}O_{V\text{-}SMOW}$ composition of surface seawater in the shallow coastal areas (−4.0‰; Zhou et al., 2020) during the early Eocene, it supports the influence of meteoric pore water. Thus, we interpret this mixed, low-ionic-strength water as the diagenetic agent responsible for the kaolinization process. However, the occurrence of intergranular pore-filling (Fig. 6f) and fracture-clogging kaolinite (Fig. 5e), as well as kaolinite co-occurring with relatively high-temperature dolomite (T_h > 100 °C) indicate multiphase kaolinization. Moreover, kaolinite sitting on the edge of pitted quartz grains (Fig. 6c) and at the embayed contact of quartz and calcite (Fig. 5a; Appendix Cf) may indicate multiple dissolution phases as well. The open-packing texture and the irregular pitted margins of detrital quartz and calcite elsewhere were interpreted to represent the result of localised quartz dissolution during early carbonate diagenesis (e.g., Worden et al., 2020). Textural observations suggest calcite replacement of quartz grains in the studied samples pointing to a similar process affecting the Eocene succession of the Hungarian Palaeogene Basin. Therefore, some kaolinite may have accumulated in pore spaces that were created by the dissolution of quartz grains or by the later

dissolution of quartz-replacing carbonates.

5.5. Burial calcite cementation and neomorphism

Besides the microspar in the matrix of the sandstone, calcite is also present as equant blocky, poikilotopic, drusy and fracture-filling cement (Fig. 5; Appendix Ce–h, Da, b, d and f), indicating a wide range of diagenetic conditions during burial history. The patchy occurrence of the poikilotopic and equigranular blocky calcite highlights the process of burial recrystallisation (Saigal and Bjørlykke, 1987), whereas the drusy nature of the calcite crystals supports an origin by direct precipitation (Morad, 1998). The fossil fragments that are stained purple to pale blue (Fig. 5f) also imply recrystallisation (dissolution and re-precipitation) of the precursor skeletons originally composed of high-magnesian calcite (cf., Richter and Füchtbauer, 1978). The stable carbon isotope values of the cm-sized euhedral mold-, oversized pore- and fracture-filling calcite are close to 0‰ (−0.54 to 1.61‰; Table 4). Bulk rock $\delta^{13}C$ values are also near 0‰ (−0.34 to 1.00‰; Table 4), which is thought to reflect a marine bioclastic source (Morad, 1998). These values together with petrographic observations, such as neomorphism of carbonate mud and recrystallisation of skeletal grains support burial recrystallisation. The negative values close to −3‰ (−2.39 to −3.83‰; Table 4) suggest that decarboxylation during thermal alteration of the organic matter was contributing to the dissolved carbon content (Morad, 1998). Marine $\delta^{13}C$ values are also supported by the presence of marine skeletal fragments, whereas the effect of organic matter diagenesis is supported by the presence of coal measures in the siltstones (Körmös et al., 2020), and solid bitumen associated with sandstones (Appendix Ca, b). The T_h of the primary aqueous FIs, trapped in equant calcite, is above 100 °C (Fig. 11) and proves that equant calcite precipitation occurred during deep burial mesodiagenesis. In some cases, the primary aqueous FIs, enclosed in equant calcite, are characterised by decreasing T_h towards the edges of the crystals, which reflects a cooling trend during precipitation likely during Pliocene uplift (Nagymarosy and Hámor, 2012).

5.6. Fracture-filling calcite cementation

Petrographic and geochemical data suggest that the various calcite cement types, such as equant, euhedral and the fracture-filling calcite formed under various conditions, even though the stable oxygen isotope composition of the euhedral calcite and sandstones-hosted equant calcite is identical (Fig. 14; Table 4). Based on the $\delta^{18}O$ of the equant calcite, the corresponding fluid inclusion T_h and the calcite-water oxygen isotope fractionation equation (O'Neil et al., 1969) suggest that the mineralizing fluid was a basinal brine characterised by a minimum $\delta^{18}O_{V\text{-}SMOW}$ value of 3.1‰.

The fracture-filling calcite is slightly depleted in ^{16}O (Fig. 14) and hosts primary aqueous FIs with lower T_h values (Fig. 11) compared to the equant and euhedral calcites. Consequently, the source formation water is characterised by $\delta^{18}O_{V\text{-}SMOW}$ values between 3.9‰ and 5.9‰ (Fig. 16), slightly higher than those of the euhedral calcite, 4.1‰ and 5.1‰ (Fig. 16). The higher $\delta^{18}O_{V\text{-}SMOW}$ and lower T_h values suggest that fracture-filling calcite postdates the euhedral one. The timing of the formation of this calcite is estimated based on the presence of primary HCFIs to have occurred sometime during the last six million years since the source rocks of the area reached the oil window within this period (Milota et al., 1995). A genetic relation of this calcite with hydrocarbon-bearing fluids is further supported by their $\delta^{13}C_{V\text{-}PDB}$ values (−0.5‰; Table 4), indicating that the migrating fluids contained dissolved carbon likely originating from thermal maturation of the organic matter at least to some extent.

5.7. Burial dissolution and kaolinite cementation

The presence of oversized and moldic pores (Fig. 5c; Appendix Ad and Da) in the sandstones that otherwise show evidence for mechanical and chemical compaction suggest burial (post-compaction) dissolution of the labile framework grains and bioclasts. This dissolution event indicates the incursion of low-pH or low-ionic-strength formation water, which dissolved the unstable framework grains. This fluid could have entered the formation either with a considerable hydraulic head (e.g., Mansurberg et al., 2020), including vertical and lateral communication (e.g., Mádl-Szőnyi et al., 2019) or could have been generated by the process of organic matter maturation (e.g., Morad, 1998). The presence of dense kaolinite replacing ductile grains with no visible intercrystalline porosity (Fig. 8d) and the continuous thermal maturation of the organic matter within the research area (Körmös et al., 2021) support the deep burial origin of the kaolinite filling some of these pores. Kaolinite is also present along dissolution pores partially cemented by medium-crystalline ferroan calcite, showing pitted margins (Appendix Cf) and, hence postdating it. Furthermore, the fracture-filling calcite embays kaolinite booklets (Fig. 5e). The presence of kaolinite and the embaying fracture-filling calcite with well-developed crystal facets suggest that the fracture system conducted chemically diverse fluids. The heterogeneous nature of the pore system, e.g., the occurring intercrystalline, oversized and biomoldic pores, points to a vital role of dissolution in reservoir quality enhancement. The observed coarse crystal size of kaolinite may reveal a slow formation at a lower level of supersaturation (McKay et al., 1995) and supports the subsequent changes in water chemistry, such as the effective concentration of elements and Eh-pH conditions. Based on mineralogical (Table 1) and petrographic (Fig. 8a) observations the textural features of kaolin crystals indicate a transformation into dickite (Morad et al., 1994) in a temperature range between 80 and 130 °C (Ehrenberg et al., 1993).

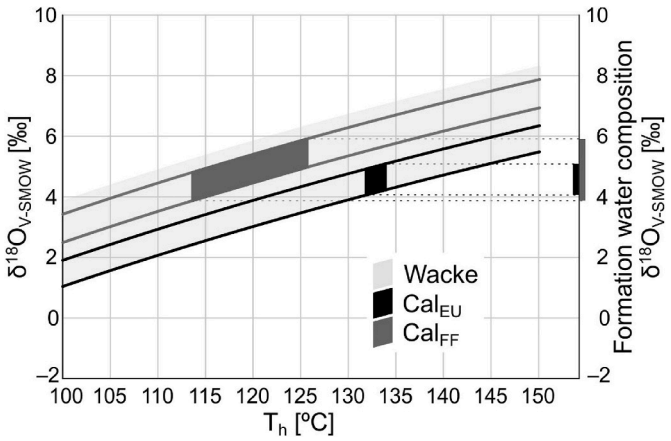

Fig. 16. Formation water composition, $\delta^{18}O_{V\text{-}SMOW}$ is based on homogenisation temperatures (Th) of FIs and stable oxygen isotope ($\delta^{18}O_{V\text{-}PDB}$) of selected carbonate phases based on O'Neil et al., 1969., Cal_{EU} – euhedral calcite, Cal_{FF} – fracture-filling calcite.

5.8. Quartz cementation

Syntaxial overgrowth and outgrowth of quartz crystals occur in the arenites. However, the lack of these quartz cements in the wackes suggests that the presence of pervasive calcite hampered quartz formation. An internal source of the silica for these cements is suggested by the evidence of pressure solution (e.g., stylolites, Fig. 8f; Appendix Ca, b; e.g., Barclay and Worden, 2000). The alteration of feldspar grains (e.g., Worden and Morad, 2003) and the progressive transformation of smectite to illite (see later; e.g., McKinley et al., 2003) possibly also contributed to the source of the quartz cement. The T_h of primary aqueous FIs along the dust rims suggests a temperature range of fluid entrapment between 110 °C and 136 °C (Fig. 11). This range of minimum trapping temperature (cf.,Goldstein and Reynolds, 1994)

corresponds well with the proposed thermal conditions of the kaolinite to dickite transformation (Ehrenberg et al., 1993), which likely accompanied quartz cementation under similar chemical conditions.

5.9. Illitisation

Locally the authigenic quartz and kaolin crystals are covered by illite and illite/smectite flakes (Fig. 7b) suggesting a diagenetic origin of the illite and illite/smectite. Illite is a product of progressive transformation of the pre-existing smectite *via* mixed-layer illite/smectite intermediate stages. Smectite to illite transformation occurs at a temperature greater than 70–90 °C (e.g., Boles and Franks, 1979; Morad et al., 2000) further supporting that the succession reached burial depths and corresponding temperatures in excess of 70–90 °C (cf., T_h in quartz; Fig. 11). Another possible source for illite is feldspar alteration (Morad et al., 2000; Worden and Burley, 2003), as indicated by the lack of feldspar (Fig. 3a) and the presence of kaolinite (Fig. 8), a likely product of feldspar alteration. Nevertheless, the low amount of illite and mixed-layer illite/smectite (Table 1) suggest that most potassium feldspar grains in the sediments were altered during earlier stages of diagenesis and were not available to supply adequate amounts of material to form larger quantities of illite and illite/smectite.

5.10. Burial dolomitization and thermochemical sulphate reduction

Even though an early-formed, potentially organogenic core is assumed to have served as nucleation sites for later dolomite growth, textural observations and FI data indicate that the bulk of the replacive and cement dolomites formed during relatively late, high-temperature diagenetic processes. For example, planar dolomite crystals are embayed by syntaxial quartz overgrowths (Fig. 7a; Appendix D) and kaolin crystals (Fig. 6f). The T_h of primary aqueous FIs enclosed in planar dolomite rhombs (105–142 °C; Fig. 11) indicates formation at elevated temperatures. Elevated formation temperatures (min. 60–80 °C) are also supported by the locally occurring saddle dolomite (Fig. 6b; e.g., Spötl and Pitman, 1998). The Mg^{2+} for these dolomites might be supplied by the alteration of clay minerals. For example, the transformation of smectite to illite, which occurs in the same temperature range in which these dolomites formed, releases a considerable amount of Mg^{2+} and Fe^{2+} that could be taken up by dolomite (Boles and Franks, 1979). Furthermore, the alteration of clay intraclasts may have contributed to Eh-pH conditions favourable for dolomite formation (e.g., Barclay and Worden, 2000). Locally appearing calcite inclusions within dolomite crystals (Fig. 7h) suggest the replacive origin of some of the dolomite. The changes in pore-fluid chemistry, e.g., the effective concentration of elements, is further documented by the chemical variation in the internal cement of well-preserved bioclasts, including purple-stained calcite in the outer chamber with a rim of blue-stained calcite and non-ferroan dolomite in the central chamber (Fig. 5d). All these show the availability of reactive Fe^{2+} and Mg^{2+} during progressive diagenetic evolution. The chemical zonation, documented by fluorescence and carbonate staining (Fig. 6a, e) along with the decreasing trend in the T_h and T_m(Ice) of AIs in the planar dolomite rhombs (Fig. 13) document the chemical evolution of the parent fluid and the incorporation of Fe^{2+}. As the petrographic observations suggest, dolomite at least partially replaced (ferroan) calcite, suggesting, at least locally, another internal source of Fe^{2+} for ferroan dolomite formation, besides the supplied cations by the alteration of clay minerals. This process also enhanced porosity since dolomite has a smaller molar volume than calcite (Warren, 2000). Calcite and dolomite cements occur in approximately equal amounts in some arenites, including pebbly sandstones (Table 4), but their crystal size did not allow mineral-selective stable isotope analyses. Nevertheless, the bulk $\delta^{13}C$ values (−0.24 to −3.83‰; Table 4), suggest that besides the reorganization of the marine bioclastic carbon source (i.e., dissolution of bioclast supplying material for carbonate cementation), decarboxylation during thermal alteration of the organic matter may also have contributed to the dissolved carbon content of the mineralizing fluids (Morad, 1998).

Besides the eogenetic pyrite framboids, pyrite crystals are associated with solid bitumen and pyrite also locally replaces quartz grains and planar dolomite rhombs (Fig. 9c and d; Appendix Dh). The presence of solid bitumen suggests a mesogenetic origin since hydrocarbon generation started six million years ago (Milota et al., 1995), ca. 35 Ma after the deposition of the host sediments. Moreover, the cogenetic HCFIs and AIs hosted in quartz minerals also document a hydrocarbon-bearing fluid migration at elevated temperatures, further supporting the burial origin of these pyrite aggregates. This temperature range (115–130 °C) is favourable for thermochemical sulphate reduction (Machel, 2001) but sulphate phases are not known in the research area. Therefore, hydrocarbons likely served as the source for H_2S generation either as a result of thermal maturation or H_2S reacted with saturated hydrocarbons forming elemental sulphur, which was later reduced. In high-temperature diagenetic conditions, sulphur acts as an active oxidizing agent for hydrocarbons, producing H_2S, solid bitumen and NSO compounds among others (Orr, 1977). Therefore, in the presence of metal cations, e.g., Fe^{2+}, pyrite forms on nucleation sites of eogenetic pyrite framboids (Machel, 2001).

5.11. Mineralizing fluid evolution during the late mesogenesis

Fluid inclusion analyses, stable oxygen isotope and detailed petrography revealed that cement minerals formed at elevated temperatures, but the source fluid chemistry differs significantly. Based on FI microthermometry the FIAs have not been subjected to thermal re-equilibration (cf., Goldstein and Reynolds, 1994, Fig. 12), and the chemical zonation of the dolomite also rules out this process (e.g., Mazzullo, 1992).

The T_h values of the cement minerals (Fig. 11) considerably overlap. Comparing these results with the petrographic observations, a prolonged period with substantial changes in fluid chemistry characterise the evolution of pore fluids that control dissolution and precipitation processes. In some cases, a decreasing trend in the T_h values can be observed towards the younger growth zones (e.g., equant calcite spar and dolomite rhomb). However, the salinity of the enclosed fluids was not following the same trend in the equant calcite spars. On the contrary, obvious changes in the salinity were recorded by dolomite rhombs, following the trend of T_h, and also documented in chemical zonation (Figs. 6e and 12). The high salinity values, recorded by AIs are typical of basinal brines in the Hungarian Palaeogene Basin (Kovács and Gyuricza, 2014). The descending trend in salinity is either the result of mixing with meteoric water present at the basin margin with an elevated hydraulic head (e.g., Khalifa et al., 2017; Poros et al., 2011) or indicate the changes in water chemistry (e.g., the effective concentration of elements evolving with progressive diagenetic processes) of the basinal fluids. The calculated $\delta^{18}O_{V\text{-}SMOW}$ values of formation water (Fig. 16) are consistent with brines described in sedimentary basins (e.g., Khalifa et al., 2017) ruling out the role of meteoric water during dolomite formation. The chemical zonation (Fig. 6a, e) indicates the variations in the concentrations of Fe^{2+} and Mg^{2+} during precipitation (Morad, 1998). The salinity values, preserved in quartz crystals hosted AIs along dust rims, show an opposite relation compared to dolomite (Fig. 12). The T_m(Ice) values increase with rising homogenisation temperatures, indicating less saline formation water. Quartz postdates dolomite and a recurrent and prolonged period of cementation can be reconstructed, in which the burial depth and temperature have a critical role on the source fluid in as much as the effective concentration of the dissolved elements, Eh-pH conditions follow the changes of salinity.

The carbonate minerals are characterised by retrograde solubility during progressive burial (Morad et al., 2000), resulting in carbonate precipitation due to a decrease in dissolved CO_2 in the pore-fluid. Organic matter-bearing mudstones are present along the basin (Fig. 2; Körmös et al., 2021) and the transformation of smectite to illite releases

a considerable amount of Mg^{2+} and Fe^{2+} (Boles and Franks, 1979) together with CO_2 as a by-product of thermal alteration of the organic matter. The dewatering of mudstone and the expulsion of CO_2 contribute to the development of the pore system by the acidic nature of the fluid front and may also be responsible for the quartz and carbonate cementation (Morad et al., 2000). The $\delta^{13}C_{V\text{-}PDB}$ values of dolomite cemented samples (Table 2) highlight the contribution of decarboxylation during thermal alteration of the organic matter to the dissolved carbon content (Morad, 1998), supporting the previous assumption.

5.12. Hydrocarbon migration

The cogenetic AIs and HCFIs in equant and fracture-filling calcite as well as in quartz mineral phase(s) indicate that hydrocarbons migrated together with the basinal brines. Besides the HCFIs studied here, Körmös et al. (2019) reported aromatic hydrocarbons, methane and CO_2, liberated from FIs trapped in bulk samples (drill cuttings) of the Kosd Formation. However, mineral selective analyses were not performed and the tightly held fluids probably also contributed to their results (cf., Volk and George, 2019). Nevertheless, methane was detected in AIs entrapped in euhedral calcite (Fig. 10). Based on the above observations, methane saturation is assumed (cf., Munz, 2001) and the aqueous phase may represent the H_2O–NaCl–$CH_4 \pm CO_2$-system, which was concluded by Poros et al., 2011 in the Buda Hills, another part of the Hungarian Palaeogene Basin.

The fluorescence colour of HCFIs ranges from yellowish to bluish colours under UV excitation (Fig. 13). These observations correspond well with previous findings (Bauer et al., 2016). Aromatic hydrocarbons and polar compounds enclosed within FIs are responsible for the fluorescence properties (e.g., Stasiuk and Snowdon, 1997). Stasiuk and Snowdon (1997) demonstrated the correlation between fluorescence and API gravities of the trapped liquids in FIs; heavy oils show emission at higher wavelengths than lighter oils. That suggests a wide range of composition of the entrapped hydrocarbons. However, the intra- and intermolecular interactions make the interpretation of the fluorescent spectra difficult (Bertrand et al., 1986). The polar compounds preferentially adsorb onto charged mineral surfaces. Thus, when captured in minerals, inclusion oils generally contain a higher proportion of polar compounds and, therefore, show a red shift relative to the associated reservoir oils (e.g., Han et al., 2022; Nedkvitne et al., 1993; Stasiuk and Snowdon, 1997). Considering the paragenetic sequence and the UV fluorescence of hydrocarbon-bearing FIAs, the equant calcite presumably trapped heavier oils, containing more polar compounds than the postdating counterparts (quartz and fracture-filling calcite). Besides the chemical composition, the thermal maturity of the inclusion oil may also affect the fluorescence properties. George et al. (2001) confirmed that blue-fluorescing HCFIs have molecular maturity anywhere in the oil window, making the maturity assumption of the investigated HCFIs controversial. Nevertheless, consequential differences in maturity are not expected because the thermal maturity of the crude oils and source rocks in the study area are in a narrow range (Körmös et al., 2021). The most probable explanation of the blue shift in UV fluorescence properties is phase separation or gas washing during or preceding trapping (Bourdet et al., 2014; Ping et al., 2019) since oil and gas generating source rocks are present in the Hungarian Palaeogene Basin (Körmös et al., 2020, 2021). Based on the above discussion, the hydrocarbon emplacement is interpreted to have occurred during a prolonged period under varying conditions, as indicated by the presence of primary HCFIs enclosed in a variety of host minerals, and the range of fluorescence colours likely represents at least a two-stage hydrocarbon charge events.

6. Conclusion

Detailed investigation of an Eocene mixed siliciclastic–carbonate succession in the Pannonian Basin led to the following conclusions. The shallow-marine depositional environment controlled the eogenetic processes. The sandy carbonate shelf provided suitable conditions for bacterial sulphate reduction. Extensive calcite cementation and neomorphism resulted in the loss of reservoir quality and lateral homogeneity. Whereas, the meteoric water incursion during sea-level lowstand at shallow burial enhanced the reservoir properties by the development of intragranular and intergranular porosity and also resulted in important vertical heterogeneity. Kaolinite formation and conversion into dickite during burial diagenesis on the one hand increased secondary porosity since it consumed feldspar and clay intraclasts but on the other hand partly reduced permeability as kaolinite clogged some of the pore spaces. Besides kaolinization, chemical compaction during increasing burial provided a sufficient source of silica for quartz cementation. The earlier alteration of feldspar resulted in a lack of potassium supply for late-diagenetic illite formation. Alteration of the basin-wide mudstones and the progressive transformation of smectite *via* mixed-layer illite/smectite to illite released a considerable amount of Mg^{2+} and Fe^{2+} for dolomite formation. Dolomite replacement may have locally improved porosity. Hydrocarbon emplacement with accompanying late pyrite formation further deteriorated porosity. The tectonostratigraphic evolution of the study area, i.e., propagation and cementation of the fault system by late ferroan calcite, contributed to improving and reducing the lateral and vertical fluid flow. These steps collectively resulted in a heterogeneous reservoir, characterising the Eocene lithology in the Hungarian Palaeogene Basin.

Credit author statement

Sándor Körmös: Conceptualization, Investigation – in general, Writing – original draft, Visualization, Writing – review & editing; **Andrea Varga**: Writing – review & editing; **Béla Raucsik**: Investigation – X-ray powder diffraction measurements, Writing – review & editing; **Georgina Lukoczki**: Writing – review & editing; **Balázs Géza Radovics**: Writing – review & editing, Formal analysis; **Nikoletta Papp**: Writing – review & editing; **István Futó**; Investigation – stable isotope measurements, **Félix Schubert**: Writing – review & editing, Supervision.

Declaration of competing interest

The authors declare that they have no known competing financial interests or personal relationships that could have appeared to influence the work reported in this paper.

Data availability

The data used to support the findings of this study are included within the article.

Acknowledgement

The authors gratefully acknowledge MOL Plc. For granting the availability of samples and permission for submitting the manuscript. We thank JMPG editor-in-chief Dr Massimo Zecchin, section editor Dr Salvatore Critelli and an anonymous reviewer for handling and commenting the original manuscript. This work was sponsored by the National Research, Development and Innovation Fund, Cooperative Doctoral Programme (975153) and Hungarian Scientific Research Fund (K-138919) Ministry for Innovation and Technology, Hungary, and the University of Szeged Open Access Fund (5860).

Appendices.

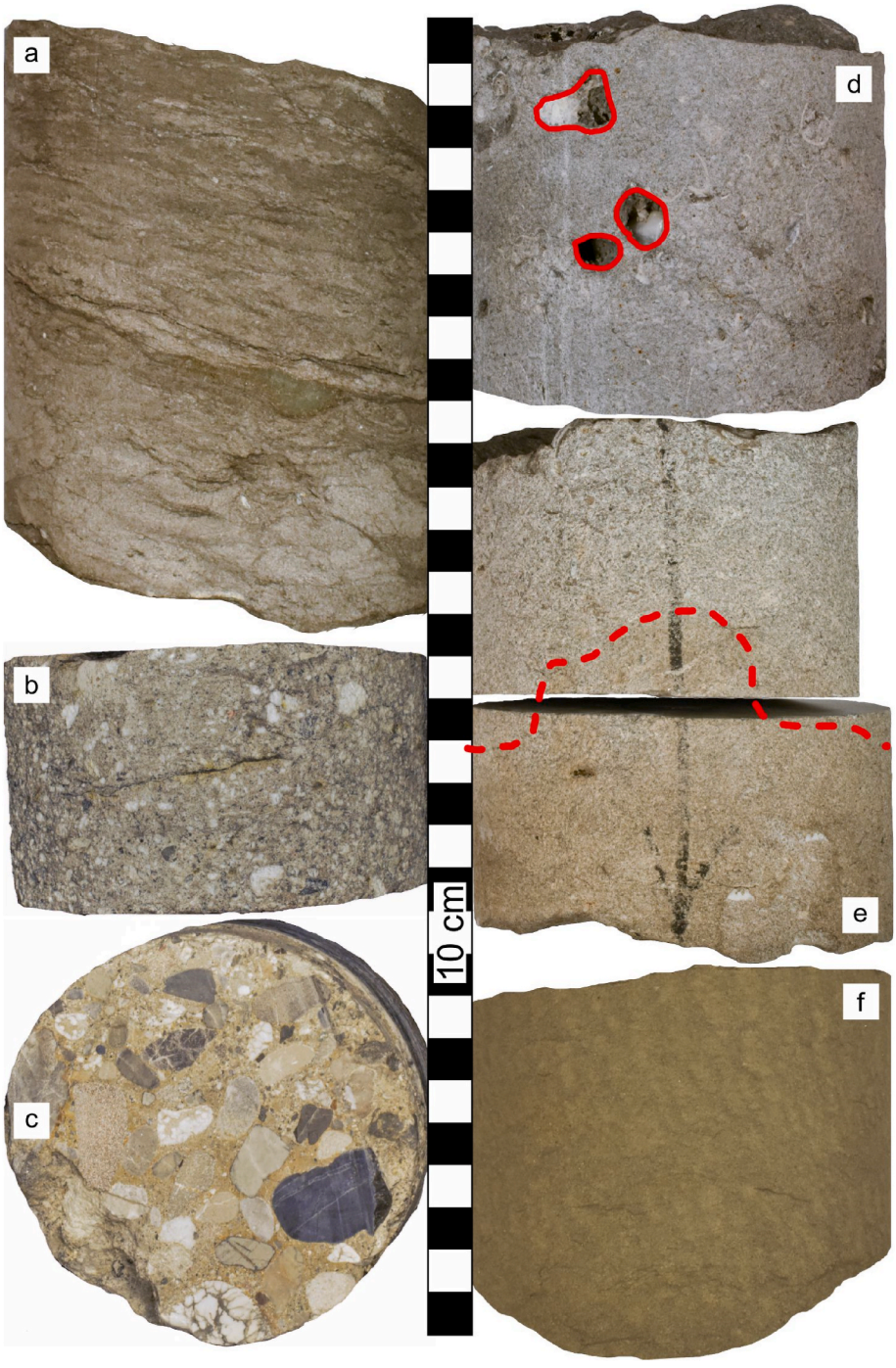

Appendix A. Representative drill cores examined for this study. a) Siltstone is interbedded with sandstone; the bedding is destroyed by bioturbation. b) Sandstone with granules and pebbles. c) Grain-supported conglomerate. d) A structureless sandstone (quartz wacke) with cm-sized biomoldic pores partially filled by calcite. Red curves highlight the moldic pores. e) The sharp contact of the thick-bedded and structureless sandstone (wacke) and oil-impregnated sandstone (arenite). The contact is highlighted by a red dashed line. f) An oil-impregnated massive and structureless sandstone (quartz arenite). (For interpretation of the references to colour in this figure legend, the reader is referred to the Web version of this article.)

Appendix B

Modal composition based on counting 400 points in each thin section, following the Gazzi-Dickinson point-counting method (Ingersoll et al., 1984) and porosity of the investigated samples (Boncz, 2013).

Well	ID	a	b	c	d	e	f	g	h	i	j	k	l	m	n	o	p	q	r	s	t	u	v	w	x
	[#]	[%]																							
Well–9	1	31.9	12.6	6.6	1.8	2.0	11.2	1.0	1.4	3.4	2.4	1.2	6.4	0.4	0.6	0.4	0.0	0.4	0.0	0.2	9.4	arg.	1.0	8.1	8.8
	2	30.3	27.3	3.4	1.0	0.4	13.7	0.8	2.6	2.0	1.2	0.4	5.0	0.0	0.2	1.2	0.0	0.2	0.0	0.4	7.5	arg.	0.0	n.d.	9.2
	3	31.1	19.2	3.4	0.6	0.2	11.8	0.2	0.4	2.0	2.2	1.4	5.4	0.0	0.2	0.8	0.0	0.0	0.4	2.0	11.4	arg.	1.8	n.d.	9.6
	4	32.8	18.3	2.6	0.4	0.0	2.4	0.4	1.6	0.4	2.2	0.8	2.6	0.8	1.0	12.9	0.0	0.0	0.4	10.9	4.2	arg.	2.2	7.4	9.1
	5	43.8	27.6	4.1	0.0	0.0	3.4	0.0	0.0	4.1	8.9	0.9	0.5	0.0	0.2	0.2	0.0	1.1	0.0	0.0	3.4	arg.	0.7	2.0	12.1
	6	37.3	32.4	3.0	0.0	0.0	5.3	0.0	0.0	3.0	6.2	1.5	1.9	0.0	0.4	0.9	0.0	1.9	0.0	0.0	4.3	arg.	1.1	4.2	9.3
	7	22.6	11.4	2.2	0.0	0.0	10.8	0.0	24.6	3.0	8.5	1.0	1.4	0.0	0.4	11.2	0.0	0.0	0.0	0.8	2.0	arg.	0.2	0.4	16.5
	8	19.1	8.4	1.2	0.2	0.0	12.2	0.0	21.1	4.2	11.4	0.8	0.6	0.0	0.2	12.7	0.0	0.0	0.0	0.6	7.4	calc.	0.0	0.5	19.9
Well–14	9	40.2	20.2	2.4	0.0	0.0	0.6	0.0	3.1	0.0	0.6	0.0	3.1	0.2	0.0	6.1	1.6	0.0	2.7	5.5	12.7	arg.±calc.	0.2	5.1	9.0
	10	38.4	15.5	2.7	0.0	0.0	0.4	0.0	3.9	0.0	0.4	0.0	4.3	0.2	0.4	7.5	1.6	0.0	4.5	5.7	14.4	arg.±calc.	0.4	8.5	9.3
	11	36.9	20.5	4.2	0.0	0.0	1.0	0.0	6.2	0.0	1.2	0.0	2.0	0.0	0.0	5.0	1.4	0.0	2.0	4.0	14.0	arg.±calc.	0.2	7.0	8.8
	12	38.0	18.1	3.9	0.0	0.0	0.6	0.0	3.7	0.0	0.4	0.0	3.7	0.2	0.2	5.5	1.0	0.0	3.5	4.9	12.8	arg.±calc.	0.4	5.6	5.9
	13	28.4	13.9	1.0	0.0	0.0	4.4	2.2	17.5	2.6	2.0	1.8	0.2	0.0	0.6	8.5	0.0	1.2	13.5	0.0	1.0	arg.	0.8	12.1	16.5
	14	29.0	12.5	2.2	0.0	0.0	4.7	1.5	18.2	0.9	0.6	0.7	2.2	0.0	0.9	9.7	0.2	1.7	10.5	0.0	2.8	arg.	1.1	n.d.	17.3
	15	26.4	14.3	1.5	0.0	0.0	3.6	1.5	17.5	1.5	1.7	0.8	1.7	0.0	1.1	6.5	0.2	2.9	14.3	0.0	2.3	arg.	1.5	11.8	15.6
	16	34.2	12.1	1.4	0.0	0.0	5.9	0.6	17.8	1.8	2.2	1.6	1.0	0.2	0.6	9.2	0.0	1.6	6.5	0.0	1.6	arg.	0.8	11.4	11.8
Well–1	17	65.5	1.0	7.5	0.1	0.0	12.7	0.0	0.0	0.2	0.3	0.0	0.9	0.1	0.8	6.5	0.2	0.0	0.0	0.5	2.9	arg.	0.8	4.3	13.2
	18	26.7	0.0	1.9	0.3	0.0	4.3	0.0	0.4	0.0	0.3	0.0	0.4	0.4	1.8	34.6	0.0	0.0	1.1	2.2	25.4	calc.	0.4	1.9	4.4
	19	19.0	2.6	4.6	0.0	0.0	6.7	0.0	0.7	0.0	0.0	0.0	0.5	0.3	1.3	33.3	0.0	0.0	0.4	3.6	26.1	calc.	0.6	1.9	4.4
	20	70.6	0.0	4.8	0.0	0.0	8.7	0.3	0.3	0.0	0.6	0.0	0.9	0.2	0.8	3.4	0.1	0.0	0.0	2.2	2.5	arg.	4.6	12.2	4.6
	21	31.4	0.0	1.6	0.0	0.0	7.1	0.3	0.4	0.0	0.4	0.0	0.6	0.1	1.1	30.7	0.0	0.0	0.3	0.5	25.2	calc.	0.5	2.4	6.0
	22	25.9	0.9	1.8	0.0	0.0	0.6	0.0	0.0	0.0	0.1	0.0	0.4	0.1	0.8	42.1	0.0	0.0	0.5	2.5	24.1	calc.	0.2	6.2	8.1
	23	17.8	1.3	3.9	0.0	0.0	3.4	0.0	0.4	0.0	0.2	0.0	1.0	0.3	0.8	40.6	0.0	0.0	0.0	2.0	28.3	calc.	0.0	6.2	8.1
	24	10.8	0.0	2.8	0.1	0.0	8.0	0.0	0.6	0.2	0.1	0.0	0.3	0.2	0.5	42.9	0.1	0.0	0.3	7.3	25.0	calc.	0.6	12.4	11.3
	25	13.3	0.0	5.7	0.0	0.0	8.7	0.0	0.9	0.0	0.0	0.0	0.3	0.1	0.5	38.3	0.1	0.0	0.4	4.9	26.4	calc.	0.4	n.d.	11.4
	26	32.0	1.9	5.5	0.0	0.0	1.4	0.0	0.0	0.1	0.4	0.0	0.6	0.0	1.6	29.3	0.1	0.0	0.0	1.4	23.7	calc.	2.0	n.d.	10.9
	27	37.1	2.1	6.7	0.0	0.0	8.7	0.8	0.3	0.2	0.0	0.0	0.9	0.2	1.1	23.3	0.0	0.0	0.0	2.1	16.4	calc.	0.0	n.d.	10.1
	28	27.5	0.6	3.6	0.0	0.0	0.6	0.0	0.9	0.0	0.0	0.0	1.2	0.1	1.7	37.6	0.0	0.0	0.0	0.7	25.3	calc.	0.1	12.4	11.3
	29	23.0	0.3	2.1	0.1	0.0	1.6	0.0	0.6	0.0	0.0	0.0	1.3	0.2	2.1	37.5	0.0	0.0	0.0	0.8	30.1	calc.	0.2	n.d.	10.3
	30	75.6	0.6	4.6	0.0	0.0	1.8	0.0	0.3	0.0	0.0	0.0	1.8	0.2	1.8	7.2	0.0	0.0	0.2	1.1	4.0	arg.+calc.	0.7	n.d.	11.1
	31	62.6	2.4	7.8	0.0	0.0	8.6	0.0	1.2	0.0	0.0	0.0	1.1	0.4	2.5	10.4	0.0	0.0	0.1	0.0	2.2	arg.+calc.	0.5	12.4	11.3
	32	47.8	3.4	7.7	0.0	0.0	5.8	0.0	0.3	0.0	0.1	0.0	1.0	0.0	2.2	14.6	0.1	0.0	0.0	3.9	3.3	arg.+calc.	9.8	12.4	11.3
	33	56.4	0.3	3.2	0.0	0.0	8.2	0.0	0.0	0.0	0.8	0.0	0.4	0.1	0.9	1.1	0.2	0.0	0.2	0.5	26.4	calc.	1.1	12.5	11.3
	34	20.1	0.8	3.6	0.3	0.0	4.8	0.0	0.5	0.0	0.0	0.0	0.3	0.1	0.6	39.7	0.0	0.0	1.3	4.9	21.4	calc.	1.1	2.6	7.1
	35	13.0	0.1	3.2	0.2	0.0	6.5	0.2	0.7	0.0	0.2	0.0	0.6	0.2	0.7	44.9	0.0	0.0	0.4	4.0	24.6	calc.	1.0	2.6	7.1
Well–1	36	39.9	2.3	5.3	0.0	0.0	6.7	0.0	0.3	0.0	0.2	0.0	1.4	0.2	1.9	18.5	0.2	0.0	0.2	2.3	19.6	calc.	0.8	2.5	10.2
	37	38.0	1.9	4.1	0.2	0.0	8.0	0.0	0.2	0.0	0.2	0.0	1.3	0.2	2.3	19.4	0.2	0.0	0.0	1.4	21.4	calc.	0.9	8.3	5.3
	38	24.5	1.4	6.3	0.3	0.0	4.0	0.2	0.5	0.0	0.0	0.0	0.6	0.2	1.4	42.9	0.0	0.0	0.3	3.2	13.4	calc.	0.6	7.2	8.4
	39	45.1	0.8	4.6	0.0	0.0	6.0	0.0	0.3	0.2	0.0	0.0	1.4	0.2	2.5	11.8	0.3	0.3	0.0	2.0	23.2	calc.	1.1	9.6	11.9
	40	40.9	1.5	9.7	0.0	0.0	2.1	0.0	0.0	0.0	0.0	0.0	3.3	0.1	5.4	7.0	0.0	0.0	0.0	0.0	30.0	calc.	0.0	3.8	10.6
	41	44.0	0.0	1.7	0.1	0.0	2.1	0.1	0.0	0.0	1.5	0.0	0.7	0.0	0.6	45.7	0.0	0.0	0.0	0.4	3.3	calc.+arg.	0.0	1.4	10.3
	42	62.2	0.0	3.9	0.0	0.0	3.1	0.0	0.0	0.0	1.3	0.0	2.2	0.2	1.8	6.5	0.0	0.0	0.0	0.0	18.4	calc.	0.0	1.9	12.4
	43	52.6	1.0	6.3	0.3	0.0	4.7	0.0	0.0	0.0	1.0	0.0	2.9	0.2	4.2	10.5	0.0	0.0	0.0	0.0	15.7	calc.	0.0	3.3	12.5
	44	50.9	0.3	5.3	0.2	0.0	2.6	0.0	0.0	0.0	1.2	0.0	3.6	0.2	3.1	16.9	0.0	0.0	0.0	0.0	15.0	calc.	0.0	3.6	12.2
	45	47.1	0.2	5.9	0.3	0.0	4.4	0.2	0.0	0.0	1.2	0.0	2.9	0.2	3.0	19.2	0.0	0.0	0.0	0.2	14.8	calc.	0.0	3.1	8.6
	46	48.8	0.9	5.1	0.2	0.0	2.0	0.0	0.0	0.0	1.6	0.0	3.3	0.2	4.4	12.3	0.0	0.0	0.0	0.2	20.9	calc.	0.0	3.3	8.2
	47	51.3	0.3	4.9	0.8	0.0	5.9	0.5	0.0	0.0	1.1	0.0	2.5	0.0	2.9	26.0	0.0	0.0	0.0	0.0	3.5	calc.+arg.	0.0	2.5	11.2
	48	37.0	0.6	4.5	0.1	0.0	1.6	0.5	0.0	0.0	1.2	0.0	2.2	0.0	6.2	24.5	0.0	0.0	0.0	0.0	19.8	calc.	0.0	3.3	3.2
	49	44.3	0.2	3.9	0.3	0.0	7.8	0.0	0.0	0.0	1.2	0.0	2.9	0.1	3.9	10.2	0.0	0.0	0.0	0.0	25.0	calc.	0.0	n.d.	7.4
	50	37.0	20.1	0.6	0.2	0.0	6.2	0.2	4.4	0.0	0.0	0.0	3.0	0.4	1.4	12.7	0.0	0.0	0.0	0.4	7.6	arg.	0.0	5.0	12.2
	51	42.8	10.8	2.0	0.2	0.0	5.2	0.0	3.0	0.0	0.0	0.0	4.2	0.4	1.0	15.1	0.0	0.0	0.0	0.6	8.4	arg.	0.0	5.0	9.8

(*continued on next page*)

Appendix B (*continued*)

Well	ID	a	b	c	d	e	f	g	h	i	j	k	l	m	n	o	p	q	r	s	t	u	v	w	x
	[#]	[%]																							
	52	47.0	6.7	1.8	0.4	0.0	8.5	0.2	1.8	0.0	0.4	0.0	4.7	0.2	1.4	16.0	0.0	0.0	0.0	0.6	5.1	arg.	0.0	2.3	10.6
	53	53.8	2.1	4.1	0.2	0.0	5.0	0.3	0.0	0.0	0.5	0.0	3.3	0.3	2.6	11.7	0.0	0.0	0.0	0.0	15.0	calc.	0.0	1.4	11.1
	54	45.6	1.2	4.4	0.2	0.0	5.8	0.3	0.2	0.0	0.0	0.0	4.8	0.3	4.9	11.8	0.0	0.0	0.0	0.0	20.1	calc.	0.0	2.7	9.2
	55	44.2	0.0	6.1	0.0	0.0	4.4	0.0	0.0	0.0	0.0	0.0	7.2	0.5	7.0	12.3	0.0	0.0	0.0	0.8	11.6	calc.±arg.	0.0	3.1	12.6
	56	42.8	0.0	6.6	0.0	0.0	2.3	0.0	0.4	0.0	0.2	0.0	9.1	0.4	6.3	5.2	0.0	0.0	0.0	0.3	21.8	calc.	0.0	n.d.	12.1
	57	44.8	0.0	3.8	0.0	0.0	7.0	0.0	0.0	0.0	0.0	0.0	8.4	0.4	8.7	9.7	0.0	0.0	0.0	0.4	15.4	calc.±arg.	0.0	2.2	12.6
	58	23.6	0.0	2.9	0.0	0.0	1.7	0.0	0.0	0.0	0.2	0.0	3.6	0.0	5.8	21.4	0.0	0.0	0.0	11.2	24.6	calc.±arg.	0.0	0.9	23.7
	59	47.8	0.0	3.6	0.0	0.0	2.5	0.0	0.0	0.0	0.2	0.0	6.3	0.3	5.3	14.2	0.0	0.0	0.0	2.0	16.4	calc.±arg.	0.0	0.3	14.2
	60	47.6	0.0	2.6	0.0	0.0	2.6	0.0	0.5	0.0	0.0	0.0	7.5	0.2	6.2	11.9	0.0	0.0	0.0	4.2	14.0	calc.±arg.	0.0	1.4	13.0
	61	41.7	0.0	3.9	0.0	0.0	2.8	0.0	0.3	0.0	0.1	0.0	6.8	0.3	4.1	12.2	0.0	0.0	0.0	9.5	15.2	calc.±arg.	0.0	0.9	9.1
	62	47.5	0.0	2.2	0.0	0.0	4.5	0.0	0.0	0.0	0.0	0.0	6.7	0.2	2.6	11.9	0.0	0.0	0.0	2.8	18.5	calc.±arg.	0.0	1.2	12.1
Well–7	63	39.0	27.7	7.8	0.4	0.0	8.1	0.4	0.6	0.6	1.0	0.0	1.7	0.0	3.3	0.0	0.0	0.0	0.0	0.0	4.5	arg.	5.0	3.6	4.2
	64	35.2	13.2	1.2	0.6	0.0	18.0	2.2	1.0	1.4	0.6	4.2	1.2	0.0	0.8	6.9	0.0	0.0	0.4	0.0	12.8	arg.±calc.	0.2	3.3	3.7
	65	37.0	12.3	0.4	0.2	0.0	5.0	0.6	0.0	0.6	0.4	0.0	4.8	0.0	3.4	13.1	0.4	0.0	0.0	0.0	20.2	arg.+calc.	0.2	2.6	8.6
	66	37.2	11.0	1.5	0.0	1.5	4.8	0.0	0.2	0.0	0.2	0.0	3.3	0.0	1.7	0.0	0.6	0.7	0.0	0.0	29.9	arg.	1.1	2.0	6.3
	67	39.5	27.2	2.4	0.0	0.0	4.8	0.0	0.0	0.0	0.6	0.2	4.4	0.0	1.8	4.4	0.0	0.0	0.0	0.0	11.7	arg.	0.6	2.6	7.1
	68	30.5	11.0	0.8	0.2	0.0	2.6	0.0	1.2	0.0	0.2	0.2	2.0	0.0	0.8	18.2	0.0	0.0	0.0	9.5	11.0	calc.±arg	0.5	0.7	9.0
	69	31.3	14.3	2.2	0.1	0.0	3.8	0.0	0.7	0.1	0.1	0.1	3.8	0.0	1.6	13.0	0.1	0.4	0.1	7.4	8.9	calc.±arg.	0.7	1.8	4.6
	70	31.4	10.3	2.8	0.2	0.0	4.8	0.0	0.9	0.2	0.2	0.2	3.7	0.0	1.5	11.2	0.3	0.3	0.0	4.9	13.8	calc.±arg.	0.9	1.3	6.4
Well–15	71	41.2	7.2	0.5	0.0	0.0	0.3	0.0	0.2	0.0	0.0	0.0	3.5	0.3	0.8	32.1	0.0	0.0	0.0	0.0	8.9	arg.+calc.	4.6	2.5	5.7
	72	53.2	24.2	1.0	0.0	0.0	2.4	0.0	0.6	0.0	1.0	0.0	2.0	0.0	2.2	1.2	0.0	0.0	4.8	0.0	4.2	calc.±arg	0.6	7.3	5.3
	73	54.2	20.9	3.2	0.0	0.0	1.7	0.0	1.3	0.0	0.4	0.0	1.1	0.0	1.7	1.9	0.0	0.0	3.8	0.0	5.2	calc.±arg	0.0	9.1	9.9
	74	63.9	12.0	1.7	0.0	0.0	1.3	0.0	0.4	0.0	0.2	0.0	4.3	0.0	3.4	2.6	0.2	0.2	2.6	0.2	5.5	calc.±arg	0.0	9.3	8.6
	75	48.5	21.3	1.2	0.0	0.0	2.5	0.0	0.2	0.0	0.0	0.0	3.9	0.0	2.9	0.7	0.5	0.0	7.1	0.0	9.0	calc.±arg	0.0	4.3	8.6
	76	54.2	20.4	2.2	0.0	0.0	2.0	0.0	1.8	0.0	0.4	0.0	0.4	0.0	2.0	4.2	0.2	0.2	3.5	0.2	5.0	calc.±arg	0.4	3.8	12.0
	77	54.0	24.0	0.9	0.0	0.0	1.6	0.0	1.1	0.0	0.0	0.0	3.0	0.0	2.1	2.3	0.5	0.5	3.4	0.5	4.3	calc.±arg	0.2	3.7	6.3
	78	61.8	19.1	1.3	0.0	0.0	0.7	0.0	0.7	0.0	0.2	0.0	3.3	0.0	2.4	1.3	0.0	0.0	2.6	0.0	4.6	calc.±arg	0.2	6.4	6.0

[a] monocrystalline quartz,
[b] polycrystalline quartz,
[c] undulose (>5°) quartz,
[d] plagioclase,
[e] potassium feldspar,
[f] metamorphic rock fragment,
[g] volcanic rock fragment,
[h] carbonate rock fragment,
[i] claystone rock fragment,
[j] chert fragment,
[k] sandstone rock fragment,
[l] mica (muscovite±biotite),
[m] heavy minerals,
[n] pyrite,
[o] diagenetic calcite,
[p] diagenetic dolomite,
[q] diagenetic quartz,
[r] diagenetic kaolin minerals,
[s] fossil fragments,
[t] matrix,
[u] type of matrix,
[v] porosity (2D),
[w] Hg-porosity,
[x] neutron porosity, arg. – argillaceous matrix, calc. – calcareous matrix, arg.+calc. – slight dominance of the argillaceous matrix, calc.+arg. – slight dominance of the calcareous matrix, arg.±calc. – mainly argillaceous matrix, calc.±arg – mainly calcareous matrix, n.d. – not determined.

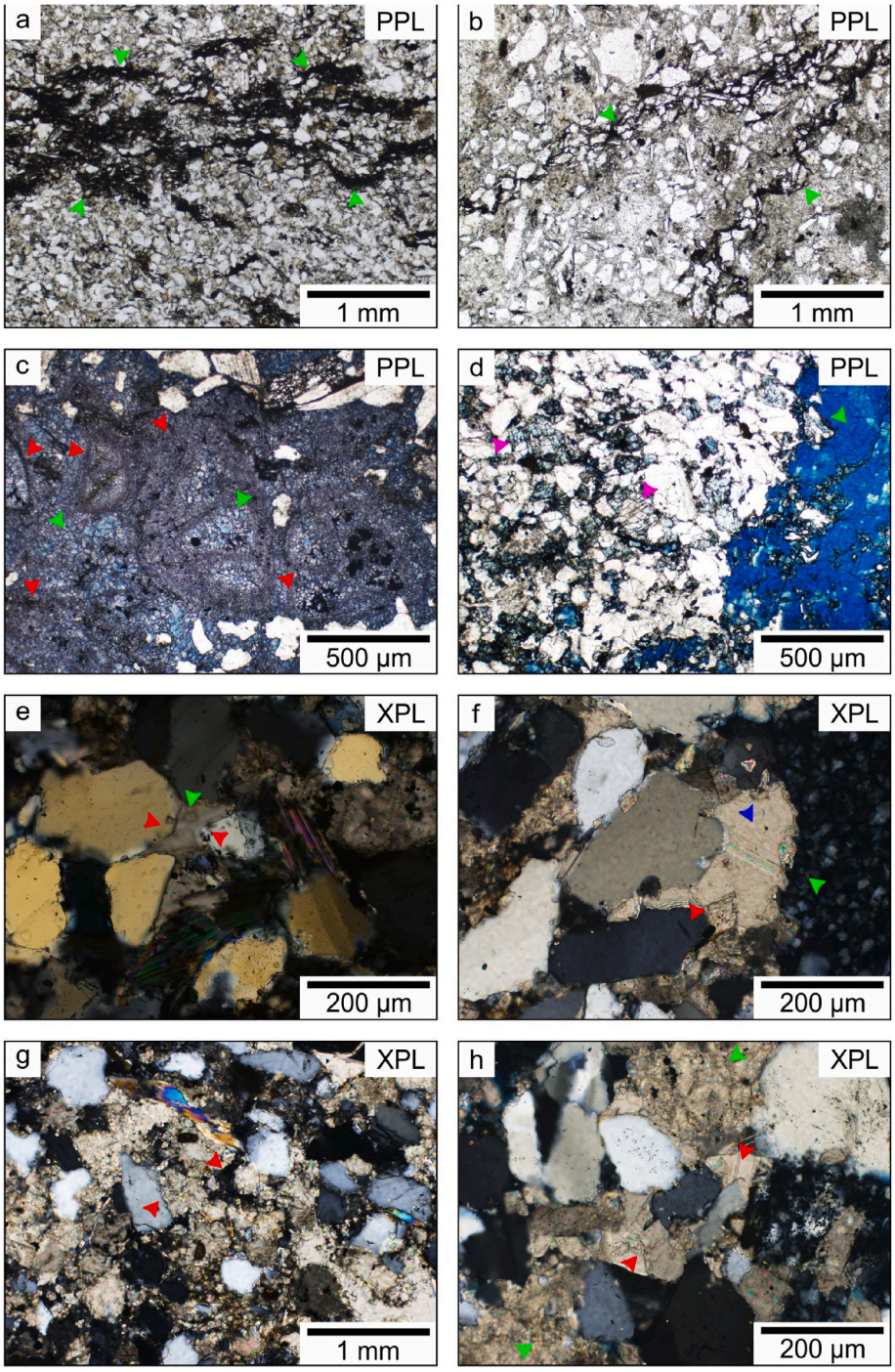

Appendix C. Photomicrographs of the investigated samples. Bitumen-impregnated dissolution seems in a) very fine-grained (W–1; 2504.1 m MD) and b) fine-to-medium-grained sandstones (W–1; 2468.1 m MD). c) Bioclasts marked by micritic envelope and purple-stained calcite (red arrows), the pore space is filled with blue-stained equant calcite (green arrows; W–1; 2461.8 m MD). d) Blue-stained ferroan calcite-filled fracture (green arrow) along with medium-crystalline and zoned, non-ferroan and turquoise-stained ferroan dolomite (purple arrows) cemented arenite (W–15; 2354.5 m MD). e) Syntaxial quartz overgrowths (red arrows) pointing towards pores, filled with calcite spar (green arrow; W–1; 2455.3 m MD). f) Calcite replaces detrital quartz grains (blue arrow), embays dolomite rhomb (red arrow) and shows pitted margins, filled with kaolin crystals (green arrow; W–1; 2455.3 m MD). g) Sparry calcite cemented arenite; red arrows point to calcite replacing detrital quartz grains. (W–15; 2354.5 m MD). h) The size of the calcite crystals changes from a micro spar (green arrows) to a medium-grained spar (red arrow; W–1; 2455.3 m MD). (For interpretation of the references to colour in this figure legend, the reader is referred to the Web version of this article.)

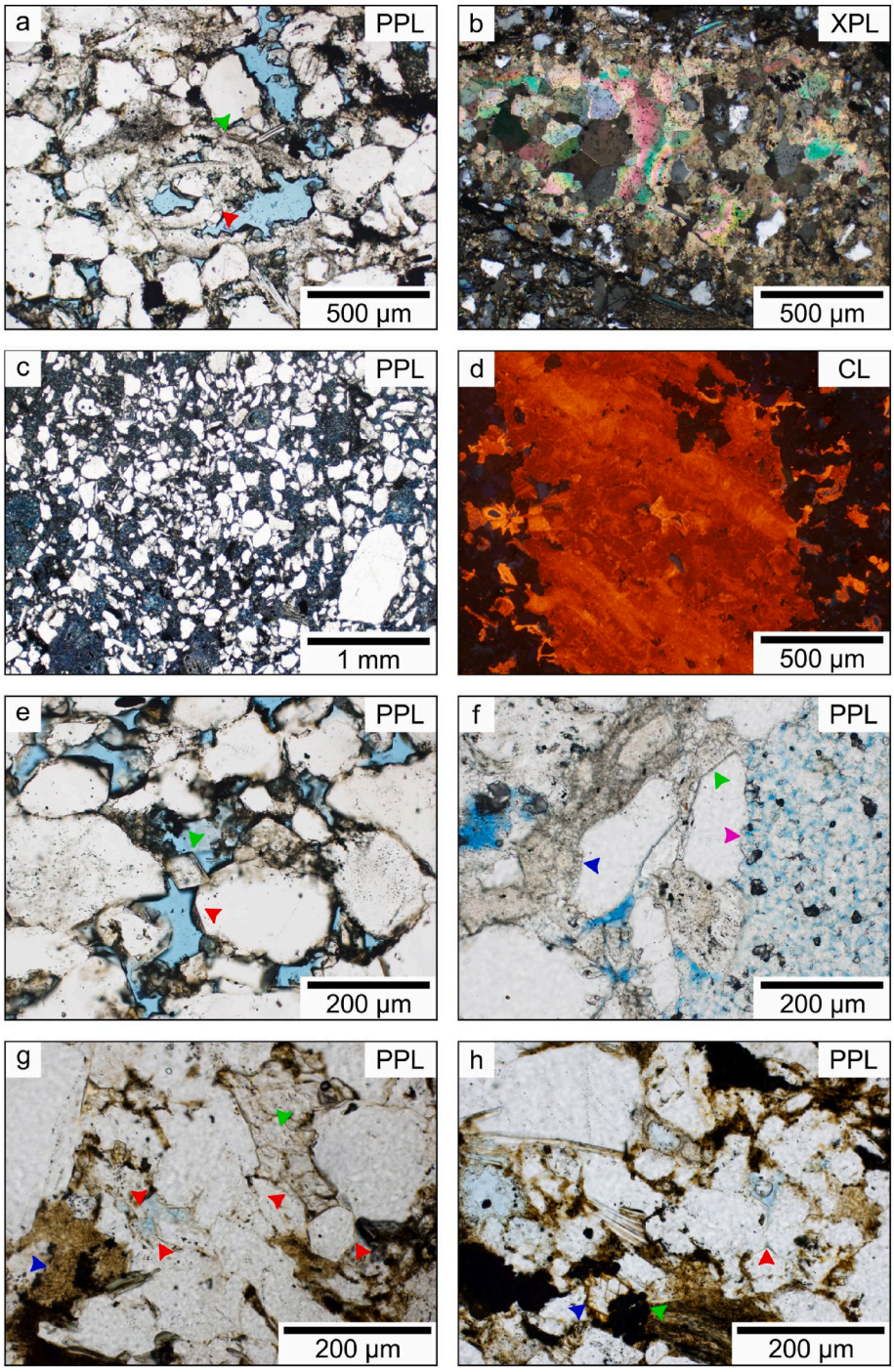

Appendix D. Photomicrographs of the investigated samples. a) Partially drusy calcite-filled biomold (red arrow). The skeletal grain is highlighted by a micritic envelope (green arrow; W–1; 2455.3 m MD). b) Drusy calcite-filled pore (W–1; 2596.8 m MD). c) Ferroan-calcite (blue-stained) cemented wacke (W–1; 2461.8 m MD). d) Orange luminescent calcite-filled fracture, showing zonation, highlighted by dull and bright bands (W–9; 2811.0 m MD). e) Quartz cement forms syntaxial overgrowths (red arrow) pointing towards pores, filled with blue epoxy. Well-developed dolomite rhombs (green arrow) are engulfed by quartz overgrowths (W–1; 2455.3 m MD). f) Calcite replaces detrital quartz grain (blue arrow), whereas kaolinite sits in embayed quartz surfaces (pink arrow). Well-developed crystal facets of quartz overgrowths are surrounded by calcite (green arrow). The same view then on Fig. 6c. (W–1; 2455.3 m MD). g) Syntaxial quartz overgrowths and discrete prismatic crystal (red arrows) pointing towards pores, filled with blue epoxy. The contacts between quartz overgrowths pointed out by brownish coloured clay minerals. Densely packed, brown kaolin crystals (blue arrow) and calcite spar (green arrow) occlude intergranular pore spaces (W–9; 2809.5 m MD). h) Syntaxial quartz overgrowths (red arrow) pointing towards pores. Subhedral pyrite crystals (green arrow) consume dolomite rhomb (blue arrow; W–9; 2810.0 m MD and 2810.5 m MD, respectively). (For interpretation of the references to colour in this figure legend, the reader is referred to the Web version of this article.)

References

Báldi, T., Báldi-Beke, M., 1985. The evolution of the Hungarian paleogene basins. Acta Geol. Hung. 28, 5–28.

Báldi-Beke, M., 2003a. A dunántúli eocén kőszénösszletek fedőképződményeinek rétegtana és paleoökológiája nannoplankton alapján (Stratigraphy and palaeoecology of the formations overlying the Middle Eocene coal sequence based

on nannofossils - (Transdanubia, Hungary)). Bull. Hung. Geol. Soc. 133, 325–343 (in Hungarian with English abstract).
Báldi-Beke, M., 2003b. A magyarországi eocén transzgressziók ideje: a nannoplankton biosztratigráfiai és magnetosztratígráfiai eredmények együttes értékelése (Time of the Eocene transgressions in Hungary: evaluation of the nannoplankton biostratigraphy and magnetostratigraphy). Bull. Hung. Geol. Soc. 133, 437–440 (in Hungarian with English abstract).
Baker, P.A., Kastner, M., 1981. Constraints on the formation of sedimentary dolomite. Science 213, 214–216. https://doi.org/10.1126/science.213.4504.214.
Bakker, R.J., 2003. Package FLUIDS 1. Computer programs for analysis of fluid inclusion data and for modelling bulk fluid properties. Chem. Geol. 194, 3–23. https://doi.org/10.1016/s0009-2541(02)00268-1.
Barclay, S.A., Worden, R.H., 2000. Geochemical modelling of diagenetic reactions in a sub-arkosic sandstone. Clay Miner. 35, 57–67. https://doi.org/10.1180/000985500546729.
Bathurst, R.G.C., 1975. Carbonate sediments and their diagenesis, second ed. Elsevier, Amsterdam.
Bauer, M., Tóth, M., Raucsik, B., Garaguly, I., 2016. Petrology and paleokarst features of the Gomba hydrocarbon reservoir (central Hungary). Centr. Eur. Geol. 59, 28–59. https://doi.org/10.1556/24.59.2016.00.
Bertrand, P., Pittion, J.-L., Bernaud, C., 1986. Fluorescence of sedimentary organic matter in relation to its chemical composition. Org. Geochem. 10, 641–647. https://doi.org/10.1016/0146-6380(86)90061-6.
Bodnar, R.J., 1993. Revised equation and table for determining the freezing point depression of H_2O-NaCl solutions. Geochem. Cosmochim. Acta 57, 683–684. https://doi.org/10.1016/0016-7037(93)90378-a.
Boles, J.R., Franks, S.G., 1979. Clay diagenesis in Wilcox sandstones of southwest Texas: implications of smectite diagenesis on sandstone cementation. J. Sediment. Petrol. 49, 55–70. https://doi.org/10.1306/212f76bc-2b24-11d7-8648000102c1865d.
Boncz, L. (Ed.), 2013. Final Report of the Hydrocarbon Exploration Activities in the Area of 138. Monor Vol. I–II. MOL Plc. Szolnok. MGSH Geological Data Store, T., Budapest, 22781 (in Hungarian).
Bourdet, J., Burruss, R.C., Chou, I.M., Kempton, R., Liu, K., Hung, N.V., 2014. Evidence for a palaeo-oil column and alteration of residual oil in a gas-condensate field: integrated oil inclusion and experimental results. Geochem. Cosmochim. Acta 142, 362–385. https://doi.org/10.1016/j.gca.2014.07.022.
Brukner-Wein, A., Hetényi, M., Vető, I., 1990. Organic geochemistry of an anoxic cycle: a case history from the Oligocene section, Hungary. Org. Geochem. 15, 123–130. https://doi.org/10.1016/0146-6380(90)90077-d.
Burley, S.D., Worden, R.H., 2003. Sandstone Diagenesis: Recent and Ancient, first ed. Blackwell Publishing, Malden, Oxford, Melbourne, Berlin.
Chiarella, D., Longhitano, S.G., Tropeano, M., 2017. Types of mixing and heterogeneities in siliciclastic-carbonate sediments. Mar. Petrol. Geol. 88, 617–627. https://doi.org/10.1016/j.marpetgeo.2017.09.010.
Coplen, T.B., 2011. Guidelines and recommended terms for expression of stable-isotope-ratio and gas-ratio measurement results. Rapid Commun. Mass Spectrom. 25, 2538–2560. https://doi.org/10.1002/rcm.5129.
Diamond, L.W., 2003. Glossary: terms and symbols used in fluid inclusion studies. In: Samson, I., Anderson, A., Marshall, D. (Eds.), Fluid Inclusions: Analysis and Interpretation. Mineral. Assoc. Can., Québec, pp. 365–374.
Dickson, J.A.D., 1965. A modified staining technique for carbonates in thin section. Nature 205, 587. https://doi:10.1038/205587a0.
Dolton, G.L., 2006. Pannonian Basin Province, Central Europe (Province 4808)–petroleum geology, total petroleum systems, and petroleum resource assessment. U. S. Geological Survey Bulletin 2204–B. https://doi.org/10.3133/b2204b.
Dott, R.H., 1964. Wacke, graywacke and matrix - what approach to immature sandstone classification. J. Sediment. Petrol. 34, 625–632. https://doi.org/10.1306/74d71109-2b21-11d7-8648000102c1865d.
Du, X., Ye, M., Xie, X., Zhao, K., Jia, J., Du, X., 2022. Why is it easy to form high-quality reservoirs in a mixed siliciclastic-carbonate system? Evidence from diagenetic characteristics. J. Pet. Sci. Eng. 212, 110339 https://doi.org/10.1016/j.petrol.2022.110339.
Ehrenberg, S.N., Aagaard, P., Wilson, M.J., Fraser, A.R., Duthie, D.M.L., 1993. Depth-dependent transformation of kaolinite to dickite in sandstones of the Norwegian continental chelf. Clay Miner. 28, 325–352. https://doi:10.1180/claymin.1993.028.3.01.
Fall, A., Tattitch, B., Bodnar, R.J., 2011. Combined microthermometric and Raman spectroscopic technique to determine the salinity of H_2O–CO_2–NaCl fluid inclusions based on clathrate melting. Geochem. Cosmochim. Acta 75, 951–964. https://doi.org/10.1016/j.gca.2010.11.021.
Feng, J., Cao, J., Hu, K., Peng, X., Chen, Y., Wang, Y., Wang, M., 2013. Dissolution and its impacts on reservoir formation in moderately to deeply buried strata of mixed siliciclastic–carbonate sediments, northwestern Qaidam Basin, northwest China. Mar. Petrol. Geol. 39, 124–137. https://doi.org/10.1016/j.marpetgeo.2012.09.002.
Flügel, E., 2004. Microfacies of Carbonate Rocks: Analysis, Interpretation and Application, first ed. Springer-Verlag, Berlin, Heidelberg.
Fodor, L., Magyari, Á., Fogarasi, A., Palotás, K., 1994. Tertiary tectonics and late Palaeogene sedimentation in the Buda Hills, Hungary. A new interpretation of the Buda line. Bull. Hung. Geol. Soc. 124, 129–305 (in Hungarian with extended English summary).
Folk, R.L., 1951. A comparison chart for visual percentage estimation. J. Sediment. Res. 21, 32–33. https://doi.org/10.1306/d4269413-2b26-11d7-8648000102c1865d.
Frezzotti, M.L., Tecce, F., Casagli, A., 2012. Raman spectroscopy for fluid inclusion analysis. J. Geochem. Explor. 112, 1–20. https://doi.org/10.1016/j.gexplo.2011.09.009.
George, S.C., Ruble, T.E., Dutkiewicz, A., Eadington, P.J., 2001. Assessing the maturity of oil trapped in fluid inclusions using molecular geochemistry data and visually-determined fluorescence colours. Appl. Geochem. 16, 451–473. https://doi.org/10.1016/S0883-2927(00)00051-2.
Gidai, L., 1978. A kósdi eocén képződmények rétegtani viszonyai (Conditions stratigraphiques des formations éocènes de Kósd). Bull. Hung. Geol. Soc. 108, 65–86 (in Hungarian with extended French summary).
Goldstein, R.H., Reynolds, T.J., 1994. Systematics of Fluid Inclusions in Diagenetic Minerals. Soc. Sediment. Geol., Tulsa https://doi.org/10.2110/scn.94.31.
Gong, Y.-M., Shi, G.R., Weldon, E.A., Du, Y.-S., Xu, R., 2008. Pyrite framboids interpreted as microbial colonies within the Permian *Zoophycos* spreiten from southeastern Australia. Geol. Mag. 145, 95–103. https://doi.org/10.1017/s0016756807003974.
Haas, J., Kovács, S., 2012. Pelso composite unit. In: Haas, J. (Ed.), Geology of Hungary. Springer-Verlag, Berlin, pp. 21–81.
Han, Y., Noah, M., Lüders, V., Körmös, S., Schubert, F., Poetz, S., Horsfield, B., Mangelsdorf, K., 2022. Fractionation of hydrocarbons and NSO-compounds during primary oil migration revealed by high resolution mass spectrometry: insights from oil trapped in fluid inclusions. Int. J. Coal Geol. 254, 103974.
Harrel, J., 1984. A visual comparator for degree of sorting in thin and plane sections. J. Sediment. Res. 54, 646–650. https://doi.org/10.2110/jsr.54.646.
Ingersoll, R.V., Bullard, T.F., Ford, R.L., Grimm, J.P., Pickle, J.D., Sares, S.W., 1984. The effect of grain size on detrital modes: a test of the Gazzi-Dickinson point-counting method. Int. J. Sediment Res. 54, 103–116. https://doi.org/10.1306/212f83b9-2b24-11d7-8648000102c1865d.
Jerram, D.A., 2001. Visual comparators for degree of grain-size sorting in two and three-dimensions. Comput. Geosci. 27, 485–492. https://doi.org/10.1016/s0098-3004(00)00077-7.
Kázmér, M., 1985. Microfacies pattern of the upper Eocene limestones at Budapest, Hungary. Ann. Univ. Sci. Budapestinensis Rol. Eotvos Nomin. Sect. Geol. 25, 139–152.
Kercsmár, Zs, Budai, T., Csillag, G., Selmeczi, I., Sztanó, O., 2015. Surface geology of Hungary. In: Explanatory Notes to the Geological Map of Hungary (1,500 000. Geological and Geophysical Institute of Hungary, Budapest.
Khalifa, M.A., Mansurbeg, H., Morad, D., Morad, S., Al-Aasm, I.S., Spirov, P., Ceriani, A., De Ros, L.F., 2017. Quartz and Fe-dolomite cements record shifts in formation-water chemistry and hydrocarbon migration in devonian shoreface sandstones, Ghadamis Basin, Libya. J. Sediment. Res. 88, 38–57. https://doi.org/10.2110/jsr.2017.66.
Kováč, M., Plašienka, D., Soták, J., Vojtko, R., Oszczypko, N., Less, Gy, Ćosović, V., Fügenschuh, B., Králiková, S., 2016. Paleogene palaeogeography and basin evolution of the Western Carpathians, Northern Pannonian domain and adjoining areas. Global Planet. Change 140, 9–27. https://doi.org/10.1016/j.gloplacha.2016.03.007.
Kovács, Zs, Gyuricza, Gy, 2014. Complex Sensitivity Report of the Monor Area, a Proposed Hydrocarbon Concession Area. Mining and Geological Survey of Hungary, Budapest (in Hungarian).
Kovács, S., Haas, J., 2010. Displaced south alpine and dinaridic elements in the mid-Hungarian zone. Cent. Eur. Geol. 53, 135–164. https://doi.org/10.1556/ceugeol.53.2010.2-3.3.
Körmös, S., Bechtel, A., Sachsenhofer, R.F., Radovics, B.G., Milota, K., Schubert, F., 2020. Petrographic and organic geochemical study of the Eocene Kosd Formation (northern Pannonian Basin): implications for paleoenvironment and hydrocarbon source potential. Int. J. Coal Geol. 103555 https://doi.org/10.1016/j.coal.2020.103555.
Körmös, S., Sachsenhofer, R.F., Bechtel, A., Radovics, B.G., Milota, K., Schubert, F., 2021. Source rock potential, crude oil characteristics and oil-to-source rock correlation in a Central Paratethys sub-basin, the Hungarian Palaeogene Basin (Pannonian basin). Mar. Petrol. Geol. 127, 104955 https://doi.org/10.1016/j.marpetgeo.2021.104955.
Körmös, S., Steinbach, G., Schubert, F., 2019. Fluid inclusion chemostratigraphy on the Eocene Kosd Formation (Central Hungary). In: Pál-Molnár, E., Berkesi, M., Guzmics, T., Kiss, B.G., Cseresznyés, D., Spránitz, T., Gelencsér, O., Király, Cs, Liptai, N. (Eds.), European Current Research on Fluid Inclusions, A Meeting Dedicated to Fluid and Melt Inclusions. Acta Mineralogica-Petrographica, p. 66.
Less, Gy, 2005. Palaeogene. In: Pelikán, P. (Ed.), Geology of the Bükk Mountains, Explanatory Book of the Geological Map of the Bükk Mountains (1:50 000). Hungarian Geological Society, Budapest, pp. 204–210.
Lucia, F.J., 2007. Carbonate Reservoir Characterization, second ed. Springer, Berlin, Heidelberg, New York.
McKinley, J.M., Worden, R.H., Ruffell, A.H., Worden, R.H., Morad, S., 2003. Smectite in sandstones: a review of the controls on occurrence and behaviour during diagenesis. In: Worden, R.H., Morad, S. (Eds.), Clay Mineral Cements in Sandstones. Blackwell Publishing Ltd, pp. 109–128. https://doi.org/10.1002/9781444304336.ch5.
Machel, H.G., 2001. Bacterial and thermochemical sulfate reduction in diagenetic settings — old and new insights. Sediment. Geol. 140, 143–175. https://doi.org/10.1016/s0037-0738(00)00176-7.
Mádl-Szőnyi, J., Czauner, B., Iván, V., Tóth, Á., Simon, S., Erőss, A., Bodor, P., Havril, T., Boncz, L., Sőreg, V., 2019. Confined carbonates – regional scale hydraulic interaction or isolation? Mar. Petrol. Geol. 107, 591–612. https://doi.org/10.1016/j.marpetgeo.2017.06.006.
Mansurbeg, H., Caja, M.A., Marfil, R., Morad, S., Remacha, E., Garcia, D., Martin-Crespo, T., El-Ghali, M.A.K., Nystuen, J.P., 2009. Diagenetic Eevolution and porosity destruction of turbiditic hybrid arenites and siliciclastic sandstones of foreland basins: evidence from the Eocene Hecho Group, Pyrenees, Spain. J. Sediment. Res. 79, 711–735. https://doi.org/10.2110/jsr.2009.060.
Mansurberg, H., Morad, S., Al Suwaidi, M., Qurtas, S., Tveiten, O.G., Shahrokhizadeh, S., Harchegani, F.K., 2020. Meteoric-water incursion into marine turbiditic sandstones: evidence from the andrew formation (paleocene), UK central graben, north sea. Mar. Petrol. Geol. 118, 104428 https://doi.org/10.1016/j.marpetgeo.2020.104428.

Mazzullo, S.J., 1992. Geochemical and neomorphic alteration of dolomite: a review. Carbonates Evaporites 7, 21–37. https://doi.org/10.1007/bf03175390.
McKay, J.L., Longstaffe, F.J., Plint, A.G., 1995. Early diagenesis and its relationship to depositional environment and relative sea-level fluctuations (Upper Cretaceous Marshybank Formation, Alberta and British Columbia). Sedimentology 42, 161–190. https://doi.org/10.1111/j.1365-3091.1995.tb01276.x.
Milota, K., Kovács, A., Galicz, Z s, 1995. Petroleum potential of the north Hungarian Oligocene sediments. Petrol. Geosci. 1, 81–87. https://doi.org/10.1144/petgeo.1.1.81.
Morad, S., 1998. Carbonate cementation in sandstones: distribution patterns and geochemical evolution. In: Morad, S. (Ed.), Carbonate Cementation in Sandstones. Blackwell Science Ltd., Cambridge, pp. 1–26. https://doi.org/10.1002/9781444304893.ch1.
Morad, S., Ismail, H.N.B., De Ros, L.F., Al-Aasm, I.S., Serrhini, N.-E., 1994. Diagenesis and formation water chemistry of Triassic reservoir sandstones from southern Tunisia. Sedimentology 41, 1253–1272. https://doi.org/10.1111/j.1365-3091.1994.tb01452.x.
Morad, S., Ketzer, J.M., De Ros, L.F., 2000. Spatial and temporal distribution of diagenetic alterations in siliciclastic rocks: implications for mass transfer in sedimentary basins. Sedimentology 47, 95–120. https://doi:10.1046/j.1365-3091.2000.00007.x.
Mount, J., 1985. Mixed siliciclastic and carbonate sediments. a proposed first-order textural and compositional classification. Sediment 32, 435–442. https://doi.org/10.1111/j.1365-3091.1985.tb00522.x.
Munz, I.A., 2001. Petroleum inclusions in sedimentary basins: systematics, analytical methods and applications. Lithos 55, 195–212. https://doi.org/10.1016/s0024-4937(00)00045-1.
Nagymarosy, A., Báldi-Beke, M., 1988. The position of the Paleogene Formations of Hungary in the standard Nannoplankton zonation. Ann. Univ. Sci. Budapestinensis Rol. Eotvos Nomin. Sect. Geol. 28, 3–25.
Nagymarosy, A., 2012. Hungarian Palaeogene Basin. In: Haas, J. (Ed.), Geology of Hungary. Springer, pp. 83–102. https://doi:10.1007/978-3-642-21910-8.
Nagymarosy, A., Hámor, G., 2012. Genesis and evolution of the Pannonian Basin. In: Haas, J. (Ed.), Geology of Hungary, pp. 149–200. https://doi:10.1007/978-3-642-21910-8_3.
Nedkvitne, T., Karlsen, D.A., Bjørlykke, K., Larter, S.R., 1993. Relationship between reservoir diagenetic evolution and petroleum emplacement in the Ula Field, North Sea. Mar. Petrol. Geol. 10, 255–270. https://doi.org/10.1016/0264-8172(93)90108-5.
O'Neil, J.R., Clayton, R.N., Mayeda, T.K., 1969. Oxygen isotope fractionation in divalent metal carbonates. J. Chem. Phys. 51, 5547–5558. https://doi.org/10.1063/1.1671982.
Orr, W.L., 1977. Geologic and geochemical controls on the distribution of hydrogen sulfide in natural gas. In: Campos, R., Gobi, J. (Eds.), Advances in Organic Geochemistry. Enadimsa, Madrid, pp. 571–597.
Ou, W., Guo, H., Lu, W., Wu, X., Chou, I.-M., 2015. A re-evaluation of the effects of temperature and NaCl concentration on quantitative Raman spectroscopic measurements of dissolved CH_4 in NaCl aqueous solutions: application to fluid inclusion analysis. Chem. Geol. 417, 1–10. https://doi.org/10.1016/j.chemgeo.2015.09.018.
Ozsvárt, P., Kocsis, L., Nyerges, A., Győri, O., Pálfy, J., 2016. The eocene-oligocene climate transition in the central paratethys. Palaeogeogr. Palaeoclimatol. Palaeoecol. 459, 471–487. https://doi:10.1016/j.palaeo.2016.07.034.
Palermo, D., Aigner, T., Geluk, M., Poeppelreiter, M., Pipping, K., 2008. Reservoir potential of a mixed carbonate/siliciclastic gas reservoir: the Lower Triassic Rogenstein in The Netherlands. J. Petrol. Geol. 31, 61–96. https://doi.org/10.1111/j.1747-5457.2008.00407.x.
Palotai, M., 2013. Oligocene−Miocene tectonic evolution of the central part of the mid-Hungarian shear zone. In: Doctoral Dissertation. Eötvös Loránd University, Budapest.
Pelikán, P., 2005. Mesozoic. In: Pelikán, P. (Ed.), Geology of the Bükk Mountains, Explanatory Book of the Geological Map of the Bükk Mountains (1:50 000). Hungarian Geological Society, Budapest, pp. 187–204.
Pettijohn, F.J., Potter, P.E., Siever, R., 1973. Sand and Sandstone, first ed. Springer-Verlag, New York, Heidelberg, Berlin.
Petrash, D.A., Bialik, O.M., Bontognali, T.R.R., Vasconcelos, C., Roberts, J.A., McKenzie, J.A., Konhauser, K.O., 2017. Microbially catalyzed dolomite formation: from near-surface to burial. Earth Sci. Rev. 171, 558–582. https://doi.org/10.1016/j.earscirev.2017.06.015.
Ping, H., Chen, H., George, S.C., Li, C., Hu, S., 2019. Relationship between the fluorescence color of oil inclusions and thermal maturity in the Dongying Depression, Bohai Bay Basin, China: Part 1. Fluorescence evolution of oil in the context of hydrous pyrolysis experiments with increasing maturity. Mar. Petrol. Geol. 100, 1–19. https://doi.org/10.1016/j.marpetgeo.2018.10.053.
Poppe, L.J., Paskevich, V.F., Hathaway, J.C., Blackwood, D.S., 2001. A laboratory manual for X-ray powder diffraction. USGS Open-File Report, Vol. 88, pp. 1–41.
Poros, Z.S., Mindszenty, A., Molnár, F., Pironon, J., Győri, O., Ronchi, P., Szekeres, Z., 2011. Imprints of hydrocarbon-bearing basinal fluids on a karst system: mineralogical and fluid inclusion studies from the Buda Hills, Hungary. Int. J. Earth Sci. 101, 429–452. https://doi.org/10.1007/s00531-011-0677-8.
Powers, M.C., 1953. A new roundness scale for sedimentary particles. J. Sediment. Petrol. 23, 117–119. https://doi.org/10.1306/d4269567-2b26-11d7-8648000102c1865d.
Radovics, B.G., Körmös, S., Schubert, F., 2017. A magyar Paleogén-medence szénhidrogén rendszere és eocén tárolóinak kihívása – hatástanulmány (The hydrocarbon system of the Hungarian Palaeogene Basin and the challenges oft he Eocene reservoirs). In: Dégi, J., Király, E., Kónya, P., Kovács, I.J., Pál-Molnár, E., Thamóné-Bozsó, E., Török, K., Udvardi, B. (Eds.), Ahol Az Elemek Találkoznak: Víz, Föld És Tűz Határán. MFGI, Budapest, pp. 147–149 (in Hungarian).
Richter, D.K., Füchtbauer, H., 1978. Ferroan calcite replacement indicates former magnesian calcite skeletons. Sedimentology 25, 843–860. https://doi.org/10.1111/j.1365-3091.1978.tb00332.x.
Saigal, G.C., Bjørlykke, K., 1987. Carbonate cements in clastic reservoir rocks from offshore Norway – relationships between isotopic composition, textural development and burial depth. In: Marshall, J.D. (Ed.), Diagenesis of Sedimentary Sequences, vol. 36. Geol. Soc. Spec. Publ, pp. 313–324. https://doi.org/10.1144/gsl.sp.1987.036.01.22.
Schmid, S.M., Bernoulli, D., Fügenschuh, B., Matenco, L., Schefer, S., Schuster, R., Tischler, M., Ustaszewski, K., 2008. The Alpine-Carpathian-Dinaridic orogenic system: correlation and evolution of tectonic units. Swiss J. Geosci. 101, 139–183. https://doi.org/10.1007/s00015-008-1247-3.
Scholle, P.A., Ulmer-Scholle, D.S., 2003. A Color Guide to the Petrography of Carbonate Rocks: Grains, Textures, Porosity, Diagenesis. AAPG, Tulsa, Oklahoma, USA. https://doi.org/10.1306/m77973.
Shepherd, T.J., Rankin, A.H., Alderton, D.H.L., 1985. A Practical Guide to Fluid Inclusion Studies. Blackie, Glasgow.
Smith, T., Guild, J., 1931. The C.I.E. colorimetric standards and their use. Trans. Opt. Soc. 33, 73–134.
Spötl, C., Pitman, J.K., 1998. Saddle (baroque) dolomite in carbonates and sandstones: a reappraisal of a burial-diagenetic concept. In: Morad, S. (Ed.), Carbonate Cementation in Sandstones. Blackwell Science Ltd., Cambridge, pp. 437–460. https://doi.org/10.1002/9781444304893.ch19.
Spötl, C., Vennemann, T.W., 2003. Continuous-flow isotope ratio mass spectrometric analysis of carbonate minerals. Rapid Commun. Mass Spectrom. 17, 1004–1006. https://doi.org/10.1002/rcm.1010.
Stasiuk, L.D., Snowdon, L.R., 1997. Fluorescence micro-spectrometry of synthetic and natural hydrocarbon fluid inclusions: crude oil chemistry, density and application to petroleum migration. Appl. Geochem. 12, 229–241. https://doi.org/10.1016/s0883-2927(96)00047-9.
Sweeney, R.E., Kaplan, I.R., 1973. Pyrite framboid formation: laboratory synthesis and marine sediments. Econ. Geol. 68, 618–634. https://doi.org/10.2113/gsecongeo.68.5.618.
Sztanó, O., Tari, G., 1993. Early Miocene basin evolution in Northern Hungary: tectonics and eustasy. Tectonophysics 261, 485–502. https://doi.org/10.1016/0040-1951(93)90134-6.
Tari, G., Báldi, T., Báldi-Beke, M., 1993. Paleogene retroarc flexural basin beneath the Neogene Pannonian Basin: a geodynamic model. Tectonophysics 226, 433–455. https://doi.org/10.1016/0040-1951(93)90131-3.
Tindall, J., Flecker, R., Valdes, P., Schmidt, D.N., Markwick, P., Harris, J., 2010. Modelling the oxygen isotope distribution of ancient seawater using a coupled ocean–atmosphere GCM: implications for reconstructing early Eocene climate. Earth Planet Sci. Lett. 292, 265–273. https://doi.org/10.1016/j.epsl.2009.12.049.
Viczián, I., 1987. Clay Minerals of the Sedimentary Rocks in Hungary. Academic Doctoral Dissertation. Hungarian Academy of Sciences, Budapest (in Hungarian).
Viczián, I., 1995. Clay minerals in Mesozoic and Paleogene sedimentary rocks of Hungary. Rom. J. Mineral. 77, 35–44.
Volk, H., George, S.C., 2019. Using petroleum inclusions to trace petroleum systems – a review. Org. Geochem. 129, 99–123. https://doi.org/10.1016/j.orggeochem.2019.01.012.
Warren, J., 2000. Dolomite: occurrence, evolution and economically important associations. Earth Sci. Rev. 1–81. https://doi.org/10.1016/s0012-8252(00)00022-2, 52.
Worden, R.H., Morrall, G.T., Kelly, S., Mc Ardle, P., Barshep, D.V., 2020. A renewed look at calcite cement in marine-deltaic sandstones: the Brent Reservoir, Heather Field, northern North Sea, UK. In: Dowey, P.J., Osborne, M., Volk, H. (Eds.), Application of Analytical Techniques to Petroleum Systems, vol. 484. Geol. Soc. London, Spec. Publ., pp. 305–335. https://doi.org/10.1144/sp484-2018-43
Worden, R.H., Burley, S.D., 2003. Sandstone diagenesis: the evolution of sand to stone. In: Burley, S.D., Worden, R.H. (Eds.), Sandstone Diagenesis: Recent and Ancient. Blackwell Publishing Ltd, pp. 1–44. https://doi.org/10.1002/9781444304459.ch.
Worden, R.H., Morad, S., 2003. Clay minerals in sandstones: controls on formation, distribution and evolution. In: Worden, R.H., Morad, S. (Eds.), Clay Mineral Cements in Sandstones. Blackwell Publishing Ltd, pp. 1–41. https://doi.org/10.1002/9781444304336.ch1.
Zhu, J., Poulsen, C.J., Otto-Bliesner, B.L., Liu, Z., Brady, E.C., Noone, D.C., 2020. Simulation of early Eocene water isotopes using an Earth system model and its implication for past climate reconstruction. Earth Planet Sci. Lett. 537, 116164 https://doi.org/10.1016/j.epsl.2020.116164.